

Experimental Study of Tsunami Generation by Three-dimensional Rigid Underwater Landslides

François Enet and Stéphan T. Grilli † M.ASCE*

Abstract: Large scale, three-dimensional, laboratory experiments are performed to study tsunami generation by rigid underwater landslides. The main purpose of these experiments is to both gain insight into landslide tsunami generation processes and provide data for subsequent validation of a three-dimensional numerical model. In each experiment a smooth and streamlined rigid body slides down a plane slope, starting from different initial submergence depths, and generates surface waves. Different conditions of wave non-linearity and dispersion are generated by varying the model slide initial submergence depth. Surface elevations are measured with capacitance gauges. Runup is measured at the tank axis using a video camera. Landslide acceleration is measured with a micro-accelerometer embedded within the model slide, and its time of passage is further recorded at three locations down the slope. The repeatability of experiments is very good. Landslide kinematics is inferred from these measurements and an analytic law of motion is derived, based on which the slide added mass and drag coefficients are computed. Characteristic distance and time of slide motion, as well as a characteristic tsunami wavelength are parameters derived from these analyses. Measured wave elevations yield characteristic tsunami amplitudes, which are found to be well predicted by empirical equations derived in earlier work, based on two-dimensional numerical computations. The strongly dispersive nature and directionality of tsunamis generated by underwater landslides is confirmed by wave measurements at gauges. Measured coastal runup are analyzed and found to correlate well with initial slide submergence depth or characteristic tsunami amplitude.

Keywords: Tsunamis; underwater landslides; laboratory tests; wave runup; surface waves.

*Now at Alkyon Hydraulic Consultancy & Research, P.O. Box 248, 8300AE Emmeloord, The Netherland.

†Department of Ocean Engineering, University of Rhode Island, Narragansett, RI 02882, USA.

Introduction

Except for the large and fortunately less frequent transoceanic tsunamis generated by large earthquake, such as the disaster recently witnessed in the Indian Ocean (e.g., Titov et al., 2005; Grilli et al., 2006), underwater landslides represent one of the most dangerous mechanisms for tsunami generation in coastal areas. While tsunamis generated by coseismic displacements are more often of small amplitude and correlate well with the earthquake moment magnitude, tsunamis generated by submarine landslides are only limited by the vertical extent of landslide motion (Murty, 1979; Watts 1998). Moreover, underwater landslides can be triggered by moderate earthquakes and often occur on the continental slope. Hence, these so-called “landslide tsunamis” offer little time for warning local populations. For instance, the consensus in the scientific community is that the 1998 Papua New Guinea tsunami, which caused over 2,000 deaths among the local coastal population, was generated by an underwater slump, itself triggered by a moderate earthquake of moment magnitude $M_s \simeq 7.1$. (Tappin et al., 2001, 2006; Synolakis et al., 2002). The large coastal hazard posed by landslide tsunamis justifies the need for identifying sensitive sites and accurately predicting possible landslide tsunami scenarii and amplitudes.

The methods used for predicting landslide tsunami amplitudes are of three main types: (i) laboratory experiments; (ii) analytical descriptions; and (iii) numerical simulations. Whereas laboratory experiments can be made quite realistic, they suffer from scale effects and are quite costly to implement, which limits the number of experiments and the relevant parameter space that can be explored. Properly validated numerical models (e.g., Grilli and Watts, 1999; Grilli et al., 2002) can advantageously complement experiments and simulate tsunamis generated by a variety of Submarine Mass Failures (SMFs), of which rigid landslides represent one idealized case. Such models have also been used to compute tsunami sources for a variety of SMFs and conduct successful case studies (Watts et al, 2003,2005; Days et al, 2005; Ioualalen et al, 2006; Tappin *et al.*, 2006).

Most of the laboratory experiments and related analytical descriptions reported so far have been done for 2D cases, either represented by solid bodies sliding down a plane slope (e.g., Wiegell, 1955; Iwasaki 1982; Heinrich, 1992; Watts, 1997, 1998, 2000; Watts et al., 2000; Grilli and Watts, 2005), or for landslides made of granular mterial (e.g., Watts, 1997; Fritz, 2002; Fritz et al., 2004). More recently, Grilli et al.

(2001), Synolakis and Raichlen (2003), Enet et al. (2003,2005), and Liu et al. (2005), presented results of 3D experiments made for rigid landslides.

A detailed discussion of numerical methods used for landslide tsunami simulations can be found in Grilli and Watts (2005), who presented results for the simulation of tsunami generation by SMFs, with a two-dimensional (2D) numerical model based on fully nonlinear potential flow equations (FNPF) (Grilli and Watts, 1999). They specifically studied underwater slides and slumps (which they treated as rotational SMFs). They validated their model using 2D laboratory experiments for semi-elliptical rigid slides moving down a plane slope and then used the model to perform a wide parametric study of tsunami amplitudes and runups, as a function of 2D SMF geometric parameters. Based on these numerical simulations, Watts et al. (2005) derived semi-empirical predictive equations for a 2D characteristic tsunami amplitude η_o^{2D} , which they defined as the maximum surface depression above the initial SMF location. Using mass conservation arguments, they further introduced corrections accounting for three-dimensional (3D) effects resulting from the finite width w of the SMFs, and derived expressions for the 3D characteristic amplitude η_o^{3D} . In parallel with these 2D simulations, Grilli and Watts (2001) and Grilli et al. (2002) applied the 3D-FNPF model of Grilli et al. (2001) to the direct simulation of 3D landslide tsunamis. The present experiments were performed in part to validate such 3D computations.

The effects of slide deformation on tsunami features, such as characteristic amplitude and wavelength, was numerically investigated by Grilli and Watts (2005). They concluded that, for both rigid and deforming 2D slides, initial acceleration is the main factor controlling tsunami source features governing far field propagation. For the moderate slide deformation rates occurring at early time, they further showed that these features were quite similar for rigid or deforming slides, although the detailed shape of generated waves differed. In fact, Watts and Grilli (2003) had earlier performed more realistic numerical computations of expanding 2D underwater landslides, represented by a modified Bingham plastic model. They had found that the center of mass motion of such highly deforming landslides was very close to that of a rigid landslide of identical initial characteristics, and most important features scaled well with and could thus be predicted, by the slide center of mass motion. Hence, for 2D landslides, more complex and realistic events can be related to a simplified rigid body motion, and vice-versa. Since deformation effects could be more important for 3D slides, however, such 2D results may not readily apply to 3D slides, but it can still be assumed that

the hypothesis of a rigid slide holds at short time.

In this work, we present results of 3D large scale laboratory experiments of tsunami generation by an idealized rigid underwater landslide, moving down a plane slope (for which partial results were reported on by Enet et al., 2003, 2005). These experiments were performed to : (1) gain physical insight into the 3D generation of tsunami and runup by underwater landslides; and (2) provide experimental data for further validating 3D numerical models, such as developed by Grilli et al. (2002). The experiments were specifically designed to validate FNPF models, although other types of models could be used as well. Therefore, the model slide was built with a very smooth and streamlined Gaussian shape, aimed at eliminating vortices and eddies not described in FNPF models. This has also led to experiments that were very repeatable and hence had small experimental errors. Other types of idealized slide geometry, such as the sliding wedge tested in Watts (1997,1998) or Liu et al. (2005) do not have these properties and hence were not considered.

At various instances in this paper, we will make reference to or use analytical or computational results, published in earlier work, in order to help better designing the experimental set-up, estimating the testable parameter space most relevant to our landslide scale model, and better interpreting the physics of landslide tsunami generation illustrated in our experimental results. In the following sections, we first detail the experimental set-up then, based on dimensional analysis, we derive and discuss analytical results, and we finally present and discuss experimental results.

Experimental set-up

General considerations

Experiments were performed in the 3.7 m wide, 1.8 m deep and 30 m long wave tank of the Ocean Engineering Department at the University of Rhode Island (URI). The experimental set-up was designed to be as simple as possible to build, while allowing to illustrate and quantify the key physical phenomena occurring during landslide tsunami generation, thus addressing goal (1) of this work. Limitations in resources also forced us to make some choices, such as building and using only one steep (i.e., shorter) plane slope and one landslide scale model geometry. We had a limited number (4) of newer precision wave gauges mounted on step motors. Other older gauges were found not accurate enough to measure the small amplitude waves

caused by deeply submerged slides. To address goal (2) of this work, as already discussed, the geometry of the experimental set-up (both slope and landslide model) was idealized in order to optimize comparisons with FNPF computations (Figs. 1, 2).

The experimental set-up thus consisted in a plane slope, 15 m long and 3.7 m wide, made of riveted aluminum plates supported by a series of very stiff I-beams. The slope was built at mid-length of the wave tank and placed at a $\theta = 15^\circ \pm 3'$ angle (Figs. 1 and 2). Upon release, the rigid landslide model translated down the slope under the action of gravity, while being guided by a narrow rail. The displacement s of the landslide parallel to the slope was obtained both from acceleration data, measured using a micro-accelerometer embedded at the slide center of mass location, and from direct measurements of the slide position, based on the time the model slide cut a piece of electric wire (later referred to as “electro-mechanical system”). Generated surface waves were measured using precision capacitance wave gauges mounted on step motors used for calibration. More details on the landslide model and instrumentation are given in the following.

Landslide model

A solid landslide model was built out of aluminum sheets, bolted and glued together in the form of a very smooth Gaussian geometry aimed at approximating sliding sediment mounds (Figs. 2 and 5). Although actual slides usually have more pronounced head shapes (e.g., Fritz, 2002), this Gaussian shape was both easier to build and deemed a close enough approximations of actual slide shapes, particularly since our goal was later to validate FNPF computations, in which the same shape could be exactly represented.

The model was set-up to move down the slope by rolling on a guiding rail, by way of stainless steel bearings in the vertical plane and teflon bearings in a plane parallel to the slope. The bearings were mounted in a cavity within the model (Fig. 3). The micro-accelerometer was also embedded within this cavity. The landslide was fitted on the rail such that its bottom slid at 4 mm above the slope. A pair of small curved springs were mounted under the slide model to prevent it from tilting and hitting the slope during motion. This experimental set-up led to a very small friction between landslide and slope, which was found in dry tests to be negligible as compared to hydrodynamic drag (less than 0.5%).

At the start of experiments, a quick release mechanism was used to let go off both the model slide

and the accelerometer cable (Figs. 3 and 6). After trying a few methods, it was found that this triggering mechanism provided the best repeatability in initial landslide acceleration. The landslide was stopped by a foam cushion placed at the bottom of the slope.

Grilli et al. (2002), in their numerical computations, defined their idealized 3D landslide geometry as having an elliptical footprint on the slope, with length b and width w , and vertical cross-sections varying according to truncated hyperbolic secant square functions, with maximum thickness T . We selected a similar geometry for our landslide model. However, to avoid changes in curvature along radial cross-sections, which would have rendered the model construction more difficult, the geometry was defined instead using truncated hyperbolic secant functions in two orthogonal directions, ξ and η (Fig. 4),

$$\zeta = \frac{T}{1 - \varepsilon} \left\{ \operatorname{sech}(k_b \xi) \operatorname{sech}(k_w \eta) - \varepsilon \right\} \quad (1)$$

with, $k_b = 2C/b$, $k_w = 2C/w$, $C = \operatorname{acosh}(1/\varepsilon)$, and $\varepsilon \in]0, 1[$, a truncation parameter.

The desired geometry was initially defined by its main dimensions (T, b, w) (Fig. 1), using $\varepsilon = 0.7$. After building and polishing the model, its dimensions were measured as $T = 0.082$ m, $b = 0.395$ m, and $w = 0.680$ m (with an absolute accuracy of 0.004 mm). Based on measurements made over a dense grid, the model external volume was calculated as, $V_b = 6.57 \cdot 10^{-3}$ m³. Weighing the model upside down underwater to ensure its central cavity would fill with water, its mass $M_b = 16.00$ Kg was measured, which gave the model bulk density $\rho_b = 2,435$ kg/m³ (smaller than aluminum 2.7 because of the water filled cavity).

For the selected geometry, the model volume can also be calculated by integrating Eq. (1), as,

$$V_b = b w T \left(\frac{f^2 - \varepsilon}{1 - \varepsilon} \right) \quad \text{with} \quad f = \frac{2}{C} \operatorname{atan} \sqrt{\frac{1 - \varepsilon}{1 + \varepsilon}} \quad (2)$$

Using the measured values of model dimensions and volume, Eq. (2) was inverted to find, $\varepsilon = 0.717$, i.e., close enough to the initially selected value. As can be seen on Fig. 2, the landslide model footprint on the slope is nearly elliptical. This can be verified by plotting Eq. (1) for $\zeta = 0$ (in dimensionless form) and comparing it to a circle, as is done in Fig. 7 where we see that differences between these are quite small (the RMS difference between both is 0.025).

Instrumentation and experimental accuracy

During experiments, landslide acceleration, displacement, free surface elevation at a few locations, and runup at the tank axis, were continuously measured at a 500 Hz frequency. The acceleration was measured with a Kystler model 8305A2M2 micro-accelerometer, embedded at the location of the model center of mass (Fig. 3) and slide displacement was obtained by double time integration. The wire connecting the accelerometer to the data acquisition system exited from the back of the landslide (Fig. 2). Since measured accelerations time series were found to be quite noisy, likely due to unwanted vibrations during slide motion, a second method was used to directly measure the slide time of passage at three selected locations on the slope. Very thin disposable copper wires, closing electric circuits, were mounted perpendicular to the slope. A small metal piece mounted on the model cut these wires during slide motion, thus opening the circuits at the precise time the slide passed by (Fig. 8). Note, this small streamlined appendix was deemed to have negligible effects on model mass and hydrodynamic characteristics.

Surface elevations were measured using four capacitance wave gauges (Brancker Research Ltd model WG-50), mounted on step motors (0.01 mm step size; Fig. 2). This allowed for frequent remote calibration of gauges, whose calibration constants were obtained by linearly curve fitting the measured gauge displacements to the recorded voltage variation. Gauge responses were found to be very linear in the measuring range ($R^2 \simeq 0.998$) and, when coating their wires with silicon to reduce meniscus effects, their absolute measurement accuracy was ~ 0.1 mm. Gauges were carefully horizontally positioned, with an accuracy of less than 1 mm (Fig. 2).

Runup was measured using a small video camera focused on the model shoreline at the tank axis (Fig. 9). A ruler taped on the slope provided a reference. After each experiment, the video recording from the camera was reviewed frame by frame, and runup was visually determined, to within approximately one millimeter.

Water depth in the tank was frequently adjusted to a constant value, $h_o = 1.500 \pm 0.001$ m. Before performing an experiment, the initial position x_i and submergence depth d of the landslide (Fig. 1) were measured using a plumb line. A metallic rod was placed on the slope to reposition the landslide within 1 mm, for successive replicates of experiments, without disturbing the free surface.

Analytical results and dimensional analysis

Landslide model law of motion

According to classical mechanics, the motion of a rigid body down a plane slope can be expressed by that of its center of mass. This approach was used in Grilli and Watts' (1999, 2005) 2D- and Grilli et al.'s (2002) 3D-models, as a so-called "wavemaker formalism", to simulate tsunami generation by SMFs. Thus, for 3D slides of similar geometry, described by a characteristic length b , width w , and thickness T , landslide motion and corresponding tsunami features can be expressed as functions of six nondimensional independent parameters : (1) a relative landslide density $\gamma = \rho_b/\rho_w$ (where ρ_w denotes water density); (2) the slope angle θ ; (3) the basal Coulomb friction coefficient $C_n = \tan \psi$; (4) a relative landslide submergence depth d/b ; (5) a relative landslide thickness T/b ; (6) and a relative landslide width w/b (Fig. 1).

Balancing inertia, gravity, buoyancy, Coulomb friction, hydrodynamic friction and drag forces, the model center of mass motion parallel to the slope, $s(t)$, is governed by (upper dots denote time derivatives),

$$(M_b + \Delta M_b) \ddot{s} = (M_b - \rho_w V_b)(\sin \theta - C_n \cos \theta) g - \frac{1}{2} \rho_w (C_F A_w + C_D A_b) \dot{s}^2 \quad (3)$$

where g is gravitational acceleration, ΔM_b , A_w , and A_b are the slide model added mass, wetted surface area, and main cross-section perpendicular to the direction of motion, respectively; C_F is a skin friction coefficient and C_D is a form drag coefficient. Eq. (3) simplifies to,

$$(\gamma + C_m) \ddot{s} = (\gamma - 1)(\sin \theta - C_n \cos \theta) g - \frac{1}{2} C_d \frac{A_b}{V_b} \dot{s}^2 \quad (4)$$

where $C_m = \Delta M_b/(\rho_w V_b)$ is the added mass coefficient of the complete system (Newman, 1989), and $C_d = C_F A_w/A_b + C_D$, is a global drag coefficient. The nature and expected magnitude of coefficients C_m and C_d are discussed in the next section. Integrating Eq. (1) for $\xi = 0$ in the η direction, we find,

$$A_b = T w \left(\frac{f - \varepsilon}{1 - \varepsilon} \right) \quad , \quad \text{and} \quad \frac{A_b}{V_b} = \frac{1}{b} \left(\frac{f - \varepsilon}{f^2 - \varepsilon} \right) \quad (5)$$

in which the model volume V_b is given by Eq. (2).

For comparison with earlier numerical results obtained for 2D landslides with semi-elliptical cross-sections, Grilli et al. (2002) introduced an equivalent semi-ellipsoid, of thickness T , length B , and width

W (Fig. 1), with lateral proportions $b/w = B/W$ and volume V_b equal to those of their landslide. The semi-ellipsoid volume is, $V_e = \pi TBW/6$ and its main cross-section, $A_e = \pi TW/2$. Thus, specifying $V_b = V_e$ and proceeding similarly, we find,

$$B = b \sqrt{\frac{6}{\pi} \frac{f^2 - \varepsilon}{1 - \varepsilon}} \quad \text{and} \quad \frac{A_e}{V_e} = \frac{1}{b} \left(\frac{3}{2} \sqrt{\frac{\pi}{6} \frac{1 - \varepsilon}{f^2 - \varepsilon}} \right) \quad (6)$$

For $\varepsilon = 0.717$, Eqs. (5) and (6) yield, $B = 0.755 b$, $A_b/V_b = 2.111/b$, $A_b = 0.03511 \text{ m}^2$, and $A_e/V_e = 1.987/b$. Hence, there is only a small difference between our model landslide and an equivalent semi-ellipsoid of identical volume and thickness, for the latter geometrical aspect parameter $\simeq 2/b$.

Integrating Eq. (4) for landslides starting at rest at time $t = 0$, with $s = 0$ and $\dot{s} = 0$, defining $\ddot{s}(0) = a_o$ and, for large times (i.e., $t \rightarrow \infty$), $\dot{s} \simeq u_t$ and $\ddot{s} \simeq 0$, we find,

$$s(t) = s_o \ln \left(\cosh \frac{t}{t_o} \right) \quad (7)$$

with the characteristic length and time of landslide motion defined as,

$$s_o = \frac{u_t^2}{a_o} ; \quad \text{and} \quad t_o = \frac{u_t}{a_o} \quad (8)$$

respectively, where,

$$a_o = g \sin \theta \left(1 - \frac{\tan \psi}{\tan \theta} \right) \left(\frac{\gamma - 1}{\gamma + C_m} \right) \quad (9)$$

is the landslide initial acceleration and, using Eq. (5),

$$u_t = \sqrt{gd} \sqrt{\frac{b \sin \theta}{d} \left(1 - \frac{\tan \psi}{\tan \theta} \right) \frac{(\gamma - 1)}{C_d} \frac{2(f^2 - \varepsilon)}{f - \varepsilon}} \quad (10)$$

is the landslide terminal velocity. With Eq. (7), the speed and acceleration of the landslide center of mass are obtained as,

$$\dot{s} = u_t \tanh \left(\frac{t}{t_o} \right) \quad \text{and} \quad \ddot{s} = a_o \cosh^{-2} \left(\frac{t}{t_o} \right) \quad (11)$$

respectively.

Based on dimensional analysis, one can also introduce a characteristic tsunami wavelength (Watts, 1998; Grilli and Watts, 2005; Fig. 1),

$$\lambda_o = t_o \sqrt{gd} \quad (12)$$

We will see that λ_o is about twice the initial tsunami wavelength.

Discussion of law of motion

Grilli and Watts (2005) used equations similar to (7)–(10) (albeit for a different geometry) to model the kinematics of 2D underwater landslides in their numerical model. They further assumed based on geotechnical considerations that, for actual landslides, once the landslide is in motion, basal Coulomb friction becomes negligible as compared to inertia, gravity, and hydrodynamic, forces. This can be expressed as, $\psi \ll \theta$ in the equations. In our landslide experiments, as indicated before, the stainless steel bearings ensure an essentially frictionless motion of the model landslide down the slope and, hence we also neglect Coulomb friction and simplify Eqs. (9) and (10) accordingly.

For 2D and quasi-2D landslides (with $w \gg b$), represented by a sliding wedge, Watts (1998,2000) experimentally found that the added mass and drag coefficients to use in equations similar to (9) and (10) were of $O(1)$ (with $\psi = 0$). Watts (1998) also indicated that, for a family of submerged landslides with similar cross-sections, C_d should be nearly constant but C_m , which more strongly depends on the flow generated around the moving landslide, should be a weak function of θ and d/b . The dependence on the latter parameters should only be significant for small values of d/b .

Considering the present landslide model is a highly streamlined symmetrical body, a locally 2D potential flow can be assumed in the downslope ξ direction and a theoretical estimate of the added mass coefficient can be made using a strip theory (e.g., Newman, 1989); thus,

$$\tilde{C}_m = \frac{\pi}{V_b} \int_0^{w/2} \zeta_{(\xi=0)}^2 d\eta \quad (13)$$

Using Eqs. (1) and (2), and integrating Eq. (13), we find,

$$\tilde{C}_m = \pi \frac{T}{b} \left\{ \frac{\sqrt{1-\varepsilon^2} - C\varepsilon(2f-\varepsilon)}{2C(f^2-\varepsilon)(1-\varepsilon)} \right\} \quad (14)$$

With $\varepsilon = 0.717$, Eq. (14) yields, $\tilde{C}_m = 2.593 T/b$, which yields 0.538, for our model.

In the experiments, for large initial slide submergence, at least two factors contributed to slightly increasing \tilde{C}_m as compared to its theoretical value. First, both the accelerometer cable and the nylon rope, used to pull the model back up the slope, were pulled by the landslide model during its motion, the com-

bined mass of which, $M_r = 0.2$ Kg led to an apparent increase, $\Delta C_{m1} = M_r/M_b = 0.0125$. Second, as indicated before, the model was set-up to roll on a rail, with its bottom located at $\delta = 4$ mm above the slope. The model footprint area on the slope can be calculated by integrating Eq. 1 for $\zeta = 0$ (Fig. 7). This yields $S_b = 0.2050$ m², and the volume of water enclosed between the slope and the model landslide is $\delta S_b = 0.82 \cdot 10^{-3}$ m³. Frictional viscous effects are large in the narrow gap δ , which means that a significant fraction (maybe 50%) of this volume, representing 12.5 % of V_b , could be entrained with the moving model slide and yield a second added mass increase by up to $\Delta C_{m2} = 0.125$; more realistically we assume 50% of this value. In conclusion, one might *a priori* expect the model slide added mass coefficient to be about, $C_m \simeq \tilde{C}_m + \Delta C_{m1} + 0.5\Delta C_{m2} \simeq 0.61$, assuming no free surface effects, i.e., a large enough relative submergence d/b . For small d/b values, one might expect a slightly larger C_m , as the free surface “resistance” to deformation will add to the inertia of the landslide model.

Based on dimensional and experimental considerations, Watts (1998, 2000) showed that, for rigid landslides, most of the tsunami generation occurs for $t \leq t_o$, a fact confirmed by Grilli and Watt’s (2005) 2D experiments. [This observation will also be well verified in the present 3D experiments.] Computations by Grilli et al. (1999, 2002) and Grilli and Watts (2005) supported this finding for both 2D and 3D cases. Over time t_o , a constantly accelerating body would move a distance,

$$s = \frac{1}{2} a_o t_o^2 = 0.5 s_o \quad (15)$$

down the slope and would reach a velocity $\dot{s} = a_o t_o = u_t$ (using Eq. (8)). Applying the more accurate Eqs. (7) to (11), we find for $t = t_o$ that $s = 0.434 s_o$, $\dot{s} = 0.762 u_t$, and $\ddot{s} = 0.420 a_o$. Hence, Eq. (15), which is the first term in the Taylor series expansion of Eq. (7), only provides a slightly larger result for $t = t_o$ than the complete equation (7). This implies that : (i) landslide initial acceleration (modeled in the present case by Eq. (9)) is the most important factor controlling tsunami generation by rigid underwater slides; (ii) hydrodynamic drag only moderately slows down landslide motion, for $t \leq t_o$. It follows that the potentially large value of the terminal velocity u_t modeled by Eq. (10), and only reached by our idealized landslide at large time (i.e., for an infinitely long slope), is much less relevant to tsunami generation and thus less important a governing parameter than a_o .

For actual slides, these results should apply to both cohesive (i.e., “rigid”) landslides and to expanding

debris flows, since the landslide expansion would be small for small times. In addition, Watts and Grilli (2003) showed that the center of mass motion of expanding landslides described by a modified Bingham plastic model is still well represented by an equation of the type (7). Finally, the plane slope approximation should also hold for more complex bottom topographies, when assuming small times and thus small slide displacements.

The expected magnitude of the global drag coefficient C_d also deserves some attention. For small T/b values, the skin friction coefficient can be estimated to be that of a flat plate in a turbulent flow (Newman, 1989),

$$C_F = \frac{0.0986}{(\log \mathbf{R} - 1.22)^2} \quad (16)$$

with $\mathbf{R} = Ub/\nu$, the flow Reynolds number, U a reference flow velocity, and ν the kinematic viscosity, about 10^{-6} m²/s for water. For small T/b values, U near the landslide model should be close at all times to the model center of mass velocity, given by Eq. (11), reaching a maximum of u_t for large time. Assuming, for simplicity, that the water velocity near the landslide model surface is around $u_t/2$ in average, and noting that we will find $u_t \simeq 2$ m/s in these experiments (Table 1), we estimate $\mathbf{R} \simeq 4 \cdot 10^5$, and $C_F \simeq 0.00514$. Now, the model wetted surface area A_w is slightly more than $2S_b = 0.41$ m². Hence, $C_F A_w/A_b \simeq 0.06$. Finally, for this slender body in a turbulent flow (large $\mathbf{R} > O(10^5)$ value), the form drag coefficient can be expected to be about $C_D = 0.3$ (the average value for ellipses of aspect ratio 2:1 to 4:1). Therefore, we find an expected minimum value of the global drag coefficient, $C_d \simeq 0.36$.

Dispersive and nonlinear effects in generated tsunamis

In designing these laboratory experiments, we found it desirable to *a priori* estimate the magnitude of dispersive and nonlinear effects in the generated tsunamis, and verify that the tested parameter space would make it possible for these effects to show up in experimental results.

Making the usual nondimensional arguments for gravity waves, one can express dispersive effects in SMF tsunamis by a relative depth parameter, $\mu = d/\lambda_o$. Assuming linear periodic waves in constant depth, a value of μ greater than ~ 0.5 indicates fully dispersive deep water waves, whereas a value of μ less

than ~ 0.05 indicates non-dispersive long waves (e.g., Dean and Dalrymple, 1991). Nonlinear effects in periodic gravity waves can be similarly expressed by a steepness parameter $\epsilon = a/\lambda_o$, where a denotes wave amplitude. In general, the smaller the value of ϵ , the more applicable linear wave theory. Specifically, Le Mehauté (1976) proposed a limit for the applicability of linear wave theory in deep water : $\epsilon < 0.0031$, with a gradual reduction of this value in intermediate water depth, as depth decreases, down to $\epsilon < 0.00017$ for the shallow water depth limit. At the other end of the range of variation of ϵ , we find an upper bound, i.e., a maximum wave nonlinearity, corresponding to the breaking limit. For deep water waves, Miche's criterion yields, $\epsilon < 0.07$, a value that is also usually assumed to decrease as a function of depth, according to a variety of empirical criteria, the simplest of which being, for very mild slopes, $2a/d \leq 0.78$ or $\epsilon \leq 0.39 \mu$, which corresponds to the maximum stable solitary wave (see, e.g., Dean and Dalrymple, 1991).

Watts et al. (2005) gave an estimate of the characteristic amplitude η_o of tsunamis caused by 3D rigid landslides, defined as the maximum depression above the landslide initial location of minimum submergence depth d (Fig. 1). This estimate applied to landslides with equivalent semi-ellipsoid dimensions (B, T, W) and was based on semi-empirical equations derived from many results of 2D fully nonlinear potential flow computations (Grilli and Watts, 1999, 2005), with an *ad-hoc* 3D correction. The characteristic amplitude scaled with s_o and was expressed as a function of five non-dimensional parameters, as,

$$\eta_o^{3D} = s_o F(\theta) G(\gamma) \left(\frac{T}{B}\right) \left(\frac{B \sin \theta}{d}\right)^{1.25} \left(\frac{1}{1 + \lambda_o/w}\right) \quad (17)$$

with the empirical functions,

$$F = 0.0486 - 0.0302 \sin \theta \quad \text{and} \quad G = 1.18 \{1 - e^{-2.2(\gamma-1)}\} \quad (18)$$

and $\theta < 30^\circ$, $T/B \leq 0.2$, $1.46 \leq \gamma \leq 2.93$, and $d/B > 0.06$. In Eq. (17), 3D amplitudes η_o^{3D} were simply obtained from the calculated 2D amplitudes η_o^{2D} by invoking mass conservation, which led to the last term, function of λ_o/w .

Following the same procedure that led to Eqs. (4) to (12), dispersion and nonlinearity parameters (μ, ϵ) can therefore be estimated for 3D landslide tsunamis as (with $\psi = 0$),

$$\mu = \frac{d}{\lambda_o} = \sqrt{\frac{d \sin \theta}{B}} \left\{ (\gamma + C_m) \sqrt{\frac{\pi}{2 C_d (\gamma - 1)}} \right\}^{-1} \quad (19)$$

and,

$$\epsilon = \frac{\eta_o^{3D}}{\lambda_o} = \left(\frac{T}{B}\right) \left(\frac{B \sin \theta}{d}\right)^{1.75} \left(\frac{1}{1 + \lambda_o/w}\right) \left\{ F(\theta) G(\gamma) \sqrt{\frac{\pi(\gamma - 1)}{2C_d}} \right\} \quad (20)$$

in which $A_b/V_b = 4/(\pi B)$ was used, based on the quasi-2D semi-elliptical landslides computations from which Eq. (17) was derived.

Eqs. (19) and (20) yield: $\mu \propto (d/B)^{0.5}$ and $\epsilon \propto (d/B)^{-1.75}$ for our experiments, which were performed over a single plane slope ($\theta = 15^\circ$), with a single landslide density ($\gamma = 2.44$), and for a single relative landslide width ($w/b = W/B = 1.72$) and thickness ($T/b = 0.21, T/B = 0.27$). This implies that, with a single landslide model, one can only simultaneously but not independently vary μ and ϵ by varying the initial submergence depth d in experiments. To vary both dispersion and nonlinearity parameters independently, one would have to use at least two landslide models with different T/B values, assuming the same density is used. More specifically, for our model, Eq. (6) yields the equivalent ellipsoid dimensions: $T = 0.082$ m, $B = 0.298$ m, and $W = 0.513$ m. Based on the above discussion, assuming $C_m \simeq 0.61$ and $C_d \simeq 0.36$ for lack of more accurate values at this stage, Eqs. (18) yields $F = 0.0408$ and $G = 1.130$, and Eq. (19), $\mu = 0.0958 (d/B)^{0.5}$.

Assuming, $w \gg \lambda_o$ to start with, i.e., quasi-2D results, Eq. (20) yields, $\epsilon = 2.27 \cdot 10^{-3} (d/B)^{-1.75}$. In this result, T/B is slightly too large for Eq. (17) to strictly apply, and $w/b = 1.72$ is quite small and hence one should expect—and we will actually observe—significant 3D tsunami generation effects in our experiments. Eq. (12) gives an estimate of λ_o , proportional to t_o , itself given by Eqs. (8) to (10). For the approximate values of C_m and C_d , we thus find $a_o = 1.20$ m/s², $u_t = 1.95$ m/s, $t_o = 1.63$ s and $\lambda_o = 5.09\sqrt{d}$.

For the submergence depths $d = 61$ to 189 mm that will primarily be tested in our experiments (Table 1), we find an average 3D amplitude correction in Eqs. (17) and (20): $\eta_o^{3D}/\eta_o^{2D} = 1/(1 + \lambda_o/w) \simeq 0.286$, which reduces the nonlinearity parameter to, $\epsilon = 6.49 \cdot 10^{-4} (d/B)^{-1.75}$ and finally yields: $\epsilon = 1.77 \cdot 10^{-7} \mu^{-3.5}$. This equation is plotted in Fig. 10, in the (μ, ϵ) nonlinearity-dispersion space, together with the limit for linear wave theory and the breaking criterion discussed above.

Watts (1998,2000) used parameter $b \sin \theta/d$ to express nonlinear effects in generated SMF tsunamis. Based on Eq. (20), this parameter reads $\{\epsilon(1 + \lambda_o/w)/0.0312\}^{1/1.75}$ for our model. Assuming the max-

imum nonlinearity value $\epsilon = 0.39 d/\lambda_o$ from the breaking criterion, we find a maximum for $b \sin \theta/d = 4.23\{d(1/\lambda_o + 1/w)\}^{0.571}$. For our model slide geometry and using Eq. (12), this leads to a submergence depth $d = 65$ mm, below which wave breaking should occur in the experiments. We have $\mu = 0.044$ for this depth, indicating initially shallow water tsunami waves (Fig. 10), and $b \sin \theta/d = 1.57$, implying a strongly nonlinear tsunami (Watts, 2000). In the experiments we found by successive trials that, for $d < 61$ mm, tsunami waves started breaking above the submerged body, which is quite close to the above predicted depth threshold. We thus selected $d = 61$ mm as the minimum submergence depth tested for non-breaking waves.

Finally, for linear wave theory to apply, the selected criterion yields (Fig. 10), $\epsilon < 0.0066 \mu - 0.00016$, and we find $b \sin \theta/d < 0.321$, or $d > 318$ mm (for which $\mu = 0.098$). Therefore, with our model slide, to fully explore nonlinear effects for non-breaking landslide tsunami generation, we should test submergence depths from $d \simeq 61$ mm to $\simeq 318$ mm. Within this depth range, generated waves would be mostly dispersive intermediate water depth waves.

Experimental results

As discussed above, in these experiments, we only tested the dependence of tsunami features on submergence depth d/b , for a single model slide and one slope angle. Seven submergence depths were tested in between $d = 61$ mm, representing the observed breaking limit, and $d = 189$ mm, the selected deepest submergence (for which tsunami characteristic amplitude was only about 3 mm; Table 1). For larger submergence depths, generated waves were too small for making accurate and repeatable measurements. An additional four experiments were performed for depths in between $d = -20$ mm (i.e., for the slide being partly emerged) and $d = 61$ mm. Tested submergence depths were spaced evenly in this interval, every 20 mm or so, except for $d = 149$ mm, due to difficulties in positioning wave gauges (Table 1).

Each experiment was repeated once. As we will see, because of the very small differences between replicates, these were averaged to reduce experimental errors. Data processing is discussed below. For $d \geq 61$ mm, gauge 1 was always located above the landslide point of minimum submergence, at $x = x_o = d/\tan \theta + T/\sin \theta$ and $y = 0$ (see Table 1), to measure $\eta(x_o, t)$ (Fig. 1), from which the characteristic tsunami amplitude is obtained as $\eta_o = \text{MAX} | \eta(x_o, t) |$. For $d < 61$ mm, there was not enough space to

locate a gauge at x_o . In all tests, the other three gauges were kept at fixed locations $(x, y) = \text{gauge 2 (1469, 350)}$; gauge 3 (1929, 0); gauge 4 (1929, 500) mm. [Note, gauges 2 and 3 were initially located symmetrically about the tank axis and, after verifying that all generated waves were symmetrical, these gauges were relocated at their final location listed above. Also note that gages 3 and 4 are located at the same x value and almost the same radial distance, 1929 and 1992 mm, from the origin of axes.] Runup R_u (i.e., maximum vertical water elevation from mean water level on the slope) was measured at the tank axis ($y = 0$) for each tested depth.

Experimental results are summarized in Table 1, and analyzed and discussed in the following.

Landslide kinematics

In each experiment, the micro-accelerometer recorded the landslide center of mass acceleration parallel to the slope as a function of time $\ddot{s}(t)$, and the electro-mechanical system measured the time of passage of the slide $t(s_{gk})$ ($k = 1, 2, 3$), at three gate locations $s_{g1} = 0.525$, $s_{g2} = 0.853$ and $s_{g3} = 1.250$ m. The measured acceleration was twice time integrated to provide slide center of mass motion. Fig. 11 shows examples of slide center of mass motion obtained from both acceleration and gate data, for two replicates of experiments performed for $d = 61, 120$, and 189 mm. These results first show that experiments are well repeatable and, second, that slide motions independently obtained from the gates and the micro-accelerometer data are in good agreement with each other.

Slide motions $s(t)$ derived from either the gate or acceleration data were used to curve fit the theoretical law of motion given by Eqs. (7) and (8), for each experiment; this yielded the slide initial acceleration a_o and terminal velocity u_t for each case. When comparing these curve fitted parameters to the raw data, it was found that the measured initial acceleration (obtained from a linear curve fit of data over a very small time, $\simeq 0.1$ s) was a more repeatable value between replicates than parameter a_o derived from the curve fitted slide motions (whether from the gate or acceleration data). Measured accelerations, however, became quite noisy for larger times (on the order of $t > 0.5t_o$), likely due to shocks and vibrations occurring during slide motion, yielding increased uncertainty for integrated slide motions and u_t derived from these through curve fitting. On the other hand, the time of passage at gates provided a more repeatable estimate of u_t

(also through curve fitting of Eqs. (7) and (8)). Hence, for each experiment, we combined the gate and acceleration data (averaged over two replicates), by using the a_o value derived from small time acceleration data and calculating the u_t value as the only parameter derived from gate data, by curve fitting Eqs. (7) and (8). Results of this combined method are given in Table 1 for all the tests. Curve fitted slide motions for the three depths mentioned above are shown on Fig. 11, on which we clearly see that the curve fits closely match the data derived from accelerations at small times but fit the gate data better at larger times.

With these results for a_o and u_t , we calculate values of t_o in Table 1 using Eq. (8), and of λ_o using Eq. (12). We see that t_o gradually increases from $d = -20$ to 140 mm and fits a linear equation, $t_o \simeq 0.900 + 7.07d$ quite well ($R^2 = 0.974$, d in meter). The two deepest submergence depths, however, do not follow this trend as u_t tends to level up maybe because of the influence of shocks that occur in deeper water at the joint between two aluminum plates in the model slope. The estimated characteristic tsunami wavelength follows the same trend as t_o , increasing from $d = -20$ to 140 mm and then stabilizing. Using this estimate and the measured values of η_o , one can calculate the locations of non-breaking experimental tests ($d \geq 61$ mm) in the (μ, ε) space. These are plotted in Fig. 10 where we see that experiments distribute about the theoretical relationship derived earlier and all correspond to dispersive intermediate water depth waves.

Eqs. (9) and (10) finally yield the C_m and C_d values for the experimental data in Table 1 (with $f = 0.8952$ for our model). The added mass coefficients C_m , expectedly, increase when d varies from partial slide emergence to shallow submergence, and then decrease to reach an average value of 0.637 for $d \geq 61$ mm, which is in good agreement with our theoretical estimate of 0.61. Values of C_d decrease from emergence to shallow submergence, to reach an average of 0.386 for $d \geq 61$, which is also in good agreement with our theoretical estimate of 0.36.

Finally, as also noted in earlier work (e.g., Watts, 1998, 2000; Grilli and Watts, 2005), Fig. 11 shows that, for $t < 0.5t_o$, slide kinematics can essentially be modeled by $s = a_o t^2/2$ or $s/s_o = 0.5t/t_o$, i.e., as a purely accelerating body that viscous drag forces have not yet significantly slowed down. Hence, the small shocks observed in experiments for later times, that affect the value of u_t , do not very much affect slide kinematics at early times.

Free surface elevations

Fig. 12 shows pictures of typical free surface elevations generated by the slide motion for $d = 61$ and 120 mm. We see a succession of cylindrical waves propagating away from the landslide initial location in the direction of its motion. A main crest can be seen, leading a train of smaller oscillatory waves. There is weaker wave propagation towards the sides of this main crest, but some of the smaller waves that follow spread slightly more laterally. This implies that there is directional focusing of most of the generated wave energy, within a fairly narrow angular sector centered about the direction of slide motion.

Pictures taken at earlier times and movies of experiments would show that, upon release of the slide model, a depression wave first forms at small times, above the initial location of the landslide, and then “rebounds” to form a main wave of elevation (i.e., the main crest) propagating offshore as a leading “N-wave” (Tadepalli and Synolakis, 1994) followed by a train of smaller oscillations (i.e., a dispersive wave tail). This will be further illustrated below based on measured surface elevations at gauges. The “rebound” wave also propagates shoreward and reflects on the slope, causing runup and some of the smaller waves seen, for instance, at the bottom of Fig. 12(b).

These processes can be better quantified by analyzing free surface elevations measured at wave gauges during landslide tsunami generation. Fig. 13 shows surface elevations measured at gauge 1, positioned at $(x_o, 0)$ above the initial slide location, and at gauge 2, downstream and off the tank axis, for the three slide depths for which landslide kinematics was analyzed in detail before (i.e., $d = 61, 120,$ and 189 mm). Some individual data points are shown for two replicates of the tests, as well as the average of those (note, small high frequency noise was filtered out). As for slide kinematics, tsunami elevations measured at gauges are well repeatable (with a maximum absolute difference of less than 1.8 mm, or 8% of the largest maximum tsunami depression); this confirms that non-systematic experimental errors are small. As expected from direct observations of experiments and from earlier 2D work (Grilli and Watts, 2005), measurements at gauge 1 essentially show a depression wave, whose maximum absolute value η_o increases as d decreases (Table 1). At gauge 2, the measured tsunami appears as a train of oscillatory waves, confirming the dispersive nature of the generated waves, with a small leading crest followed by a larger depression wave and then the highest crest. Measured wave heights are also larger at gauge 2, the shallower the initial slide submergence

depth d .

To compare all the initial tsunami sources generated at gauge 1 for $d \geq 61$ mm, measured surface elevations are plotted in Fig. 14 in non-dimensional form $(\eta/b, t/t_o)$. In this plot, for better consistency, t_o was calculated from the curve fit $t_o \simeq 0.900 + 7.07d$, which only affects the two deepest submergences depths, where a slight inconsistency in t_o value was observed. Surface elevations appear very similar at gauge 1 for all cases, in the form of simple depressions of the water surface, essentially created for $t < 0.5t_o$. This confirms that the initial landslide tsunami source, responsible for a large part of the subsequent wave generation and propagation, is produced at early times, when slide motion is that of a purely accelerating body. Therefore, initial slide acceleration a_o truly is the most important parameter for underwater landslide tsunami generation, whereas u_t only plays a secondary role. Similar conclusions were reached by Grilli and Watts (2005) based on 2D computations.

Measurements at gauge 1 represent near-field landslide tsunami sources, on which dispersive effects have not yet acted. Fig. 15, shows dimensionless elevations measured at gauges 2, 3, and 4 for $d = 61$, 120 and 189 mm, which are examples of far field landslide tsunamis. In each case, the tsunami appears as a well developed train of oscillatory waves, indicative of strong dispersive effects; a large depression wave is preceded by a small leading elevation wave (about 4 times smaller), and followed by the largest elevation wave in the train (slightly larger than the depression wave). Thus, the salient feature of these tsunamis is a so-called leading N-wave. As noted before, the tsunami amplitude is larger, the shallower the initial slide submergence. Gauges 2,3 and 4 are located at radial distances $r = 1510, 1929$, and 1992 mm, respectively, from the origin of the coordinate system. Gauges 2 and 4 have an azimuth of $\phi = 13.4$ and 14.5 degree, respectively, with respect to the tank axis. Measurements at gauge 3, which is on the tank axis, show the largest tsunamis, despite the gauge being almost the farthest from the origin. Waves are much smaller at the nearer gauge 2, and at gauge 4, which is at about the same radial distance as 3 but off the axis. This is consistent with our observations of a directional tsunami (Fig. 12).

It is of interest to measure the period T of the leading “N-wave” in the far-field tsunami. We did so in Table 1, for the first and largest oscillatory wave recorded at the farthest gauge on the axis (gauge 3); T was defined as twice the time interval spanning from the first trough to the first crest in the record (e.g., Fig. 15). Results show that this period is almost exactly $0.5 t_o$ for $d \leq 120$ mm and slightly less for deeper initial

slide submergences, maybe due to the shorter distance of propagation to gauge 3, preventing the tsunami to fully develop its far-field characteristics. [The relationship $T/t_o \simeq 0.5$ was also experimentally observed by Watts (1998, 2000) for tsunamis created by 2D sliding wedges.] For the characteristic tsunami wavelength defined in Eq. (12), we thus find the characteristic tsunami celerity as, $c_o \simeq 2\lambda_o/t_o = 2\sqrt{gd}$. This celerity is plotted in Fig. 16 as a function of d , together with the observed average tsunami celerity \bar{c} between gauges 1 and 3, obtained by dividing the distance between the gauges, $x_3 - x_o$, by the time interval between the first (small) leading elevation wave passing by gauge 3 and $t(\eta_o)$, the time the maximum surface depression occurs at gauge 1. We see in the figure that \bar{c} agrees reasonably well with c_o .

Finally, it is of interest to compare the measured characteristic tsunami amplitudes η_o to η_o^{3D} , predicted by empirical Eqs. (17) and (18), based on earlier computational work (Watts et al., 2005). This is done in Table 1 and in Fig. 17, for $d \geq 61$ mm. In the empirical equations, we used λ_o and s_o as predicted by Eqs. (8) to (12), with the known model slide geometry parameters (b, T, w, ϵ) , density γ , experimental slope θ , but with the theoretically estimated values of hydrodynamic coefficients $C_m = 0.61$ and $C_d = 0.36$, i.e., no hydrodynamic measurements from experiments were used. The overall agreement is quite good between the measured and estimated characteristic amplitudes (the correlation coefficient is $r = 0.98$), confirming the relevance of the empirical predictive equations proposed by Watts et al. (2005). The largest discrepancy is observed for the shallowest depth of 61 mm, which, as we shall all see in the next section regarding runups, is also smaller than the reference depth $d_{ref} = B \sin \theta = 77$ mm defined by Grilli and Watts (2005) (i.e., the vertical extension of the equivalent ellipsoidal slide on the slope).

Runup

Fig. 18a shows the tsunami runup R_u measured at $y = 0$ in the tank as a function of the nondimensional submergence depth d/d_{ref} . Results are shown for experiments in Table 1 with $d \geq 20$ mm. Error bars are marked on the figure, based on estimates of experimental errors discussed earlier. Errors are relatively larger for the deeper submergence depths, which yield the smallest runup. As in 2D computations by Grilli and Watts (2005), we find two different runup regimes, approximately, for shallower or deeper submergence depth than d_{ref} . Power curve fits : $R_u/b = A (d/d_{ref})^B$ are plotted in the figure for both regimes. For

$d/d_{ref} < 1$, i.e., the shallower cases (both submerged and emerged), we find $B = -0.63$ and for $d/d_{ref} > 1$, the deeper cases, $B = -1.27$. These exponents are larger than those obtained in 2D computations by Grilli and Watts (2005), as would be expected when 3D wave energy spreading occurs. In the shallower cases, both emerged and submerged, nonlinear effects are larger, which increases runup in absolute terms. However, these are also cases where wave breaking and hence energy dissipation occur. Hence, runup increases with decreasing depth, at a smaller rate B for the shallower cases than for the deeper cases.

Knowing that the empirical equation for η_o^{3D} has been globally validated in Fig. 17, one can also specifically verify that the dependence of η_o on submergence depth, the only independent parameter left in these experiments, is such as predicted in Eq. (17). This is done in Fig. 18b, where a power fit to the nondimensional data $(\eta_o/b, d/d_{ref})$ yields an exponent -1.29, i.e., quite close to the ‘‘Green’s law’’ exponent of -1.25 found in Eq. (17). These results also mean that $R_u/b \propto (\eta_o/b)^C$, with $C \simeq 1$ for the deeper cases and $C \simeq 0.5$ for the shallower cases. Hence, we find a nearly linear correspondence between runup and tsunami characteristic amplitude when the slide initial submergence is deeper ($d/d_{ref} > 1$). For shallower slides ($d/d_{ref} < 1$), the runup increases with $\sqrt{\eta_o}$. [However, only two data points are available for η_o in this region.] Similar conclusions were reached by Grilli and Watts (2005) and Watts et al. (2005), based on computations and performing a few case studies.

Summary and conclusions

We presented 3D laboratory experiments of tsunami generation by a rigid landslides, of idealized Gaussian shape, moving down a 15 degree slope. Experiments were performed in a large scale wave tank, wide enough to allow for 3D propagation of the initial tsunami to occur without being perturbed by sidewall reflection. The observed directional nature of the generated tsunamis further increased the time window for which there was no contamination of results by reflection. This allowed us to neglect sidewall effects on free surface measurements.

In each experiment, performed for a specified submergence (or emergence) depth d , we measured the slide kinematics and recorded surface elevations at 4 gauges and runup at the tank axis, generated by the slide motion. Different conditions of wave non-linearity, from strong to mild, resulted from varying the initial submergence depth from the observed breaking limit (about $d = 61$ mm) to a deeper value. All

generated waves were dispersive intermediate water depth waves. Experimental errors were quite small (0.1 mm accuracy on surface elevation measurements), and results were highly repeatable between replicates (less than 1.8 mm or 8% maximum difference). All experiments nevertheless were repeated twice and results averaged before conducting further analyses.

For each test, measured landslide acceleration and times of passage at three locations down the slope were used to curve fit an analytical law describing the slide center of mass motion. This yielded a characteristic time of motion t_o , and the slide added mass and drag coefficients. Slide motion was observed to be essentially that of a purely accelerating body for $t \leq 0.5t_o$, and most of the initial tsunami source generation occurred for small time $t < t_o$, in the form of a surface depression. This implies that the slide initial acceleration is a more important parameter for tsunami generation than the slide terminal velocity.

Measured characteristic tsunami amplitudes η_o , defined as maximum initial surface depressions, are well predicted by the empirical equation derived in earlier work, based on numerical computations (Grilli and Watts, 2005 and Watts *et al.*, 2004). Hence this further validates work on tsunami case studies performed using landslide tsunami sources calculated with these empirical equations (Watts *et al.*, 2003; Days *et al.*, 2005; Ioualalen *et al.*, 2006;). The dependence of η_o on d is specifically verified to be a power relationship similar to that computed by Grilli and Watts (2005) for 2D landslide tsunamis, with nearly Green's law -1.25 exponent. In the far field, the measured tsunamis all appear to be dispersive trains of directional oscillatory waves, with leading N-waves. The period of the N-waves is about $0.5t_o$ in most cases. Using the defined characteristic wavelength, a characteristic tsunami celerity c_o is derived which, in our experiments, agrees reasonably well with the average speed of tsunami propagation from the initial location to the farthest gauge on the axis. The strong directionality of landslide generated tsunamis may be explained in part by a near resonance occurring between the speed of slide motion down the slope and the celerity of the generated waves. For instance, in the experiments, the limiting slide speed u_t is found to be nearly equal to the characteristic tsunami celerity c_o (this can be verified in Table 1 and Fig. 16 for $d \leq 140$ mm; the last two values of u_t are suspect because of shocks down the slope, as discussed before). Measured coastal runup are found to follow power laws of d , with different exponents in two submergence depth regimes delimited by a reference depth d_{ref} , representing the vertical expansion of the slide on the slope. We finally find that there is a direct correspondence between runup and the characteristic tsunami amplitude η_o . In the deeper region,

we actually find, $R_u \propto \eta_o$, i.e., a direct proportionality between these. A similar behavior was observed by Grilli and Watts (2005) in computations of 2D tsunami landslides.

The present work was performed in part with the objective of providing benchmark data for validating landslide tsunami models, such as developed by the authors. Experimental validation of the 3D-FNPF model by Grilli et al. (2002) and of its earlier 2D version (Grilli and Watts, 1999) was performed only based on 2D experiments (Watts et al., 2000; Grilli and Watts, 2001, 2005). Data from 3D experiments reported here will thus allow for a full 3D validation of this model. This will be presented in a continuation of this work, together with sensitivity analyses of tsunami features to 3D effects (such as slide width; Enet and Grilli, in preparation).

Regarding the relevance of this work to actual landslide tsunami events, strictly speaking, our rigid slide experiments would model the behavior of cohesive landslides rather than 3D debris flows. The latter would be better modeled using small particles (e.g., Fritz et al., 2004). Earlier work indicates however that using a rigid slide does not significantly restrict our ability to model real events, made of much more complex material moving over more complicated bathymetry (Watts and Grilli, 2003; Watts et al., 2003; Grilli and Watts, 2005). This is in part due to the importance of the slide initial acceleration and small time motion for tsunami generation, as discussed above and already noted by Watts (1998), hence, at a time when slide deformation is still moderate. Regarding the bottom topography, since we showed that most of the tsunami generation occurs for small times as compared to the characteristic time of slide motion, and thus for relatively small landslide displacements, the “local” plane slope approximation holds as a representation of more complex bottom topographies.

Acknowledgments

The research reported here was supported by grant CMS-0100223 from the National Science Foundation. The late Cliff Astill, NSF Program Director at the time, is gratefully remembered for his continuing support of landslide tsunami research and for funding the author’s project. The authors are also grateful for productive discussions with, and suggestions made, by Dr. P. Watts, Applied FLuids Engng. Inc., regarding the design of the experimental set-up. Finally, the authors gratefully acknowledge the constructive comments

and suggestions made by anonymous reviewers, that helped improve the paper readability.

References

- Dean, R.G. and Dalrymple, R.A. (1991). *Water Wave Mechanics for Engineers and Scientists*. Advanced Series on Ocean Engineering - Vol II. World Scientific, Singapore.
- Day, S. J. , P. Watts, S. T. Grilli and Kirby J.T. (2005). “Mechanical Models of the 1975 Kalapana, Hawaii Earthquake and Tsunami.” *Marine Geology*, **215**(1-2), 59-92.
- Enet, F., and Grilli, S. T., and Watts, P. (2003). “Laboratory experiments for tsunamis generated by underwater landslides: comparison with numerical modeling.” *Proc. of the 13th Offshore and Polar Engrg. Conf.* (ISOPE03, Honolulu, Hawaii), ISOPE, Cupertino, CA, 3, 372-379.
- Enet F. and Grilli S.T. (2005). “Tsunami Landslide Generation: Modelling and Experiments”. In *Proc. 5th Intl. on Ocean Wave Measurement and Analysis* (WAVES 2005, Madrid, Spain, July 2005), IAHR Publication, paper 88, 10 pps.
- Fritz, H.M. (2002). “Initial Phase of Landslide Generated Impulse Waves.” *PhD Dissertation*, Swiss Federal Institute of Technology Zürich.
- Fritz, H.M., Hager, W.H. and H.-E. Minor (2004). “Near Field Characteristic of Landslide Generated Impulse Waves.” *J. Wtrwy, Port, Coast, and Oc. Engrg.*, **130**(6), 287-302.
- Grilli, S.T., Guyenne, P. and Dias, F. (2001). “A fully nonlinear model for three-dimensional overturning waves over arbitrary bottom.” *Intl. J. Numer. Meth. in Fluids*, **35**(7), 829-867.
- Grilli, S.T., Ioualalen, M, Asavanant, J., Shi, F., Kirby, J. and Watts, P. (2006). “Source Constraints and Model Simulation of the December 26, 2004 Indian Ocean Tsunami.” *J. of Waterway Port Coastal and Ocean Engineering* (this issue, in press).
- Grilli, S. T., Vogelmann, S., and Watts, P. (2002). “Development of a 3D numerical wave tank for modeling

- tsunami generation by underwater landslides." *Engrg. Analysis with Boundary Elements*, **26**(4), 301-313.
- Grilli, S. T., and Watts, P. (1999). "Modeling of waves generated by a moving submerged body: Applications to underwater landslides." *Engrg. Analysis with Boundary Elements*, **23**(8), 645-656.
- Grilli, S. T., and Watts, P. (2001). "Modeling of tsunami generation by an underwater landslide in a 3D numerical wave tank." *Proc. of the 11th Offshore and Polar Engrg. Conf.* (ISOPE01, Stavanger, Norway), ISOPE, CUperitino, CA, 3, 132-139.
- Grilli, S. T., and Watts, P. (2005). "Tsunami Generation by Submarine Mass Failure Part I : Modeling, Experimental Validation, and Sensitivity Analyses." *J. Wtrwy, Port, Coast, and Oc. Engrg.*, **131**(6), 283-297.
- Heinrich, P. (1992). "Nonlinear water waves generated by submarine and aerial landslides." *J. Wtrwy, Port, Coast, and Oc. Engrg.*, **118**(3), 249-266.
- Ioualalen, M., Pelletier, B. , Watts, P., and M. Regnier (2006). "Numerical modeling of the 26th November 1999 Vanuatu tsunami." *J. Geophys. Res.*, **111**, C06030, doi:10.1029/2005JC003249.
- Iwasaki, S. (1982). "Experimental study of a tsunami generated by a horizontal motion of a sloping bottom." *Bull. Earth. Res. Inst.*, **57**, 239-262.
- Le Mehauté, B. (1976) *An Introduction to Hydrodynamics and Water Waves*. Springer Verlag, 332 pps.
- Liu, P. L.-F., Wu, T.-R., Raichlen, F., Synolakis, C.E. and Borrero, J.C., (2005). "Runup and rundown generated by three-dimensional sliding masses." *J. Fluid Mech.*, **536**, 107-144.
- Murty, T. S. (1979). "Submarine slide-generated water waves in Kitimat Inlet, British Columbia." *J. Geoph. Res.*, **84**(C12), 7,777-7,779.
- Newman, J.N. (1989). *Marine Hydrodynamics*. The MIT Press, Cambridge, MA.

- Synolakis, C. E., Bardet, J. P., Borrero, J. C., Davies, H. L., Okal, E. A., Silver, E. A., Sweet, S., and Tappin, D. R. (2002). "The slump origin of the 1998 Papua New Guinea tsunami." *Proc. Royal Soc., London*, **458**(2020), 763-790.
- Synolakis, C.E. and Raichlen, F. (2003). "Waves and Runup Generated by a Three-dimensional Sliding Mass." In *Submarine Mass Movements and Their Consequences* (J. Locat and J. Mienert Eds.), Kluwer Academic Publishers, Dordrecht, p. 113-119.
- Tadepalli, S. and Synolakis, C. E. (1994). "The Runup of N-waves on Sloping Beaches.", *Proc. Royal Soc. London*, **445**(1923), 99-112.
- Tappin, D.R., Watts, P., McMurtry, G. M., Lafoy, Y., and Matsumoto, T. (2001). "The Sissano, Papua New Guinea tsunami of July 1998 – Offshore evidence on the source mechanism." *Marine Geology*, **175**, 1-23.
- Tappin, D.R., Watts, P. and Grilli, S.T. (2006). "The Papua New Guinea tsunami of 1998: anatomy of a catastrophic event." *Natural Hazards and Earth System Sciences* (submitted).
- Titov, V.V., Rabinovich, A.B., Mofjeld, H.O., Thomson, R.E., González, F.I. (2005). "The Global Reach of the 26 December 2004 Sumatra Tsunami." *Science*, **309**(5743), 2045-2048.
- Watts, P. (1997). "Water waves generated by underwater landslides." *PhD Dissertation*, California Inst. of Technol., Pasadena, CA.
- Watts, P. (1998). "Wavemaker curves for tsunamis generated by underwater landslides." *J. Wtrwy, Port, Coast, and Oc. Engrg.*, ASCE, **124**(3), 127-137.
- Watts, P. (2000). "Tsunami features of solid block underwater landslides." *J. Wtrwy, Port, Coast, and Oc. Engrg.*, ASCE, **126**(3), 144-152.
- Watts, P., and Grilli, S. T. (2003). "Underwater landslide shape, motion, deformation, and tsunami generation." *Proc. of the 13th Offshore and Polar Engrg. Conf. (ISOPE03, Honolulu, Hawaii)*, ISOPE, Cupertino, CA, 3, 364-371.

- Watts, P., S. T. Grilli, J. T. Kirby, G. J. Fryer, and Tappin, D. R. (2003). "Landslide tsunami case studies using a Boussinesq model and a fully nonlinear tsunami generation model." *Natural Hazards and Earth System Sciences*, **3**, 391-402.
- Watts, P., Grilli, S. T., Tappin, D.R. and G.J. Fryer (2005). "Tsunami Generation by Submarine Mass Failure Part II : Predictive Equations and Case Studies." *J. Wtrwy, Port, Coast, and Oc. Engrg.*, **131**(6), 298-310.
- Watts, P., Imamura, F., and Grilli, S. T. (2000). "Comparing model simulations of three benchmark tsunami generation cases." *Sci. Tsunami Hazards*, **18**(2), 107-124.
- Wiegel, R. L. (1955). "Laboratory studies of gravity waves generated by the movement of a submarine body." *Trans. Am. Geophys. Union*, **36**(5), 759-774.

Appendix I: Table and Figures

d (mm)	-20	0	20	40	61	80	100	120	140	149	189
x_o (mm)	NA	NA	NA	NA	551	617	696	763	846	877	1017
η_o (mm)	NA	NA	NA	NA	13.0	9.2	7.8	5.1	4.4	4.2	3.1
η_o^{3D} (mm)	NA	NA	NA	NA	15.5	9.8	6.4	5.3	4.3	3.2	2.4
R_u (mm)	12.2	15.5	13.2	8.8	6.2	5.7	4.4	3.4	2.3	2.7	2.0
a_o (m/s ²)	1.34	1.21	1.18	1.23	1.12	1.21	1.19	1.17	1.14	1.20	1.21
u_t (m/s)	0.97	1.09	1.25	1.39	1.70	1.64	1.93	2.03	2.13	1.94	1.97
t_o (s)	0.73	0.90	1.07	1.13	1.42	1.36	1.62	1.74	1.87	1.62	1.63
λ_o (m)	NA	NA	0.474	0.708	1.096	1.201	1.606	1.883	2.190	1.955	2.217
C_m	0.447	0.756	0.861	0.723	0.607	0.582	0.632	0.685	0.767	0.607	0.582
C_d	1.626	1.286	0.986	0.796	0.473	0.509	0.367	0.332	0.302	0.364	0.353
T/t_o	NA	NA	NA	NA	0.51	0.50	0.50	0.49	0.42	0.43	0.41

Table 1: Measured tsunami characteristic amplitude η_o (at $x = x_o$ and $y = 0$) and runup R_u , as a function of submergence depth d for model landslide: $b = 0.395$ m, $T = 0.082$ m, $w = 0.680$ m (averages of two replicates were made for each experiment). [Non-breaking waves were observed for $d \geq 61$ mm.] η_o^{3D} is the predicted amplitude from Eqs. (17) and (18). Slide kinematics parameters a_o , u_t , and t_o are obtained by curve fitting accelerometer and electro-mechanical system data with Eqs. (7) and (8); C_m and C_d are obtained from Eqs. (9) and (10); λ_o is obtained from Eq. (12) (with $c_o \simeq 2\lambda_o/t_o$); T is the period of the N-wave leading the “far field” tsunami measured at gauge 3. NA: Non-applicable.

List of figure captions

Figure 1: Vertical cross-section for tsunami landslide experiments, with indication of key geometrical parameters. The Gaussian shape landslide model has length b , width w , and thickness T and is initially located at $x = x_i$ at a submergence depth d . The dashed shape represents an equivalent semi-ellipsoidal landslide of same thickness and volume, length B and width W . Figure 2: General view of experimental set-up with : slope, rail, landslide model, wave gauges/step motors, and supporting I-beams.

Figure 3: Vertical cross-section in experimental set-up (heights are exaggerated).

Figure 4: Vertical cross-sections in landslide model geometry defined by Eq. (1) with $\varepsilon = 0.717$. Dimensions are specified in meter.

Figure 5: View of landslide model cross sections during construction.

Figure 6: View of model quick release mechanism.

Figure 7: (—) Half of landslide model horizontal footprint geometry, defined by Eq. (1) for $\zeta = 0$, with $\varepsilon = 0.717$, $\xi' = 2\xi/b$ and $\eta' = 2\eta/w$. (- - - -) represents a half circle.

Figure 8: View of model displacement measuring system.

Figure 9: View of video camera used to measure runoff.

Figure 10: Estimated testable parameters in tsunami landslide experiments. (o) actual values tested in experiments (with λ_o estimated with Eq. (12)). BC: breaking criterion; LWT: Linear Wave Theory; SW: Shallow Water waves; IW: Intermediate Water depth waves.

Figure 11: Measured landslide kinematics for $d = 61$ (a), 120 (b), 189 (c). Results are based on micro-accelerometer data for run: 1 (— - —), 2 (- - -); or based on electro-mechanical gate data for run: 1 (o), 2 (Δ). Curve fit (—) of Eq. (7) and purely accelerating motion $s/s_o = 0.5 t/t_o$ (— —), based on Table 1 data (as explained in text), are shown on each figure.

Figure 12: Examples of experimental surface elevations generated for $d = 61$ mm (a) and 120 mm (b), at $t \simeq t_o$. Note, the model slide is visible underwater at the top of figure (b).

Figure 13: Measured surface elevations at gauges : 1 (a) and 2 (b), for $d = a$: 61, b: 120, c: 189 mm, for run: 1 (o) and 2 (Δ). Average of both runs (—). Gauge 1 is located at $x = x_o$ and $y = 0$ (Table 1), and gauge 2 at $x = 1469$ and $y = 350$ mm. In (a), every 20 data points are shown, and in (b), every 50.

Figure 14: Measured surface elevations (averages of runs 1 and 2) at gauge 1, at $x = x_o = d / \tan \theta + T / \cos \theta$ and $y = 0$ for experiments in Table 1 with $d =$ a: 61, b: 80, c: 100, d: 120, e: 140, f: 149, g: 189 mm. Characteristic times are obtained from $t_o \simeq 0.900 + 7.07d$.

Figure 15: Measured surface elevations (averages of runs 1 and 2) at gauges: 2 (a); 3 (b); 4 (c), for experiments in Table 1 with $d =$ 61 (—), 120 (- - - -), 189 (— - —). Characteristic times are obtained from $t_o \simeq 0.900 + 7.07d$. gauge coordinates (r, ϕ) (mm,deg.) : 2 (1510,13.4), 3 (1929,0), 4 (1992,14.5).

Figure 16: Measured average tsunami celerity \bar{c} (\circ) between gauges 1 and 3, compared to characteristic tsunami celerity c_o (—), for experiments in Table 1 with $d \geq 61$ mm.

Figure 17: Measured tsunami characteristic amplitudes η_o in meter (\circ), compared to empirical predictions η_o^{3D} (Eqs. (17) and (18)), for experiments in Table 1 with $d \geq 61$ mm.

Figure 18: Landslide tsunami runup R_u (a) and characteristic amplitude η_o (b), as a function of submergence depth (with $d_{ref} = 77.2$ mm), for experiments in Table 1 (\circ), with $d \geq 20$ and 61 mm, respectively. Estimated error bars are marked for runups. Power curve fits to the data are shown (—).

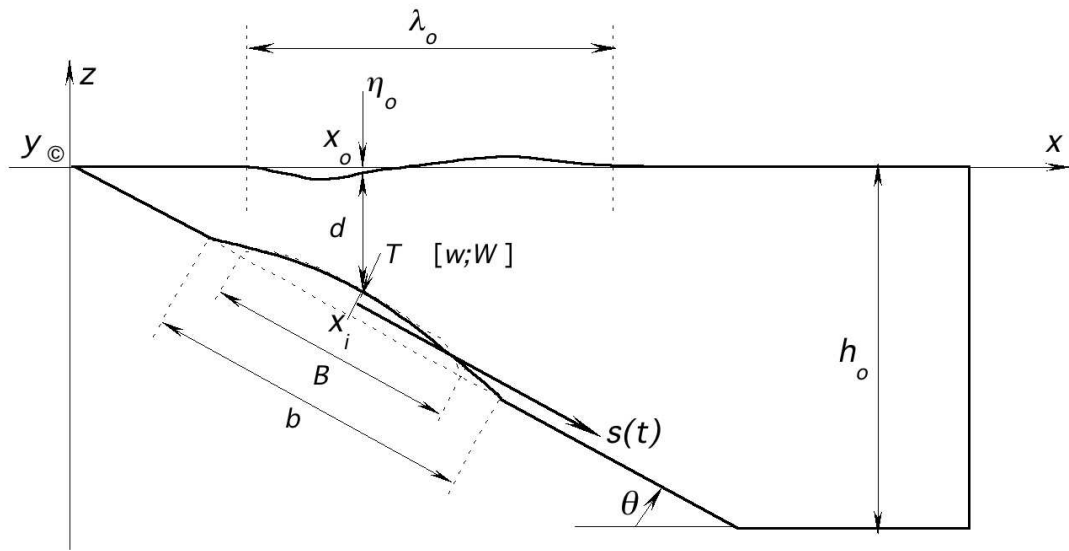


Figure 1:

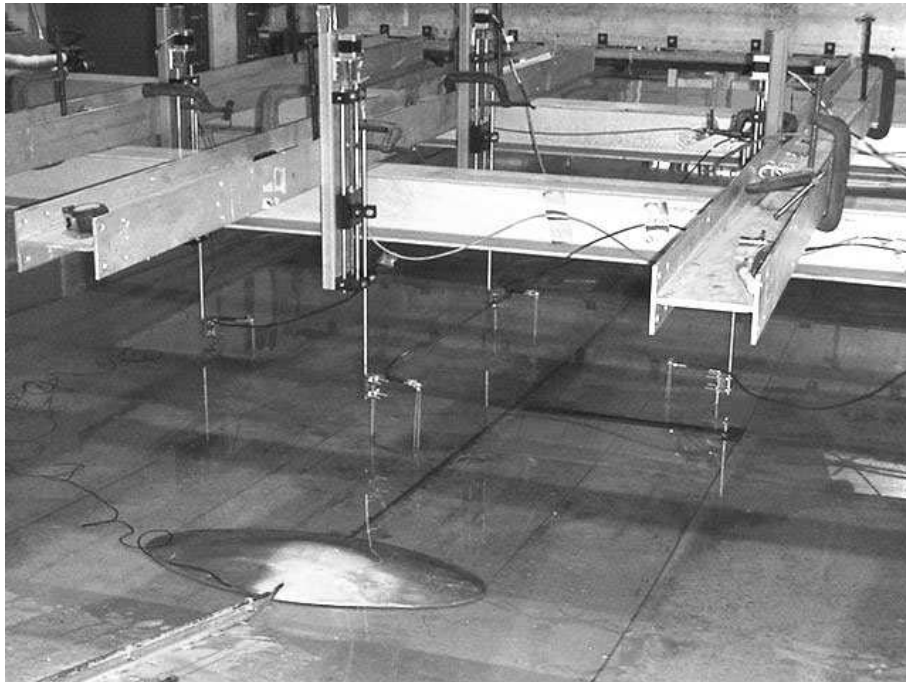


Figure 2:

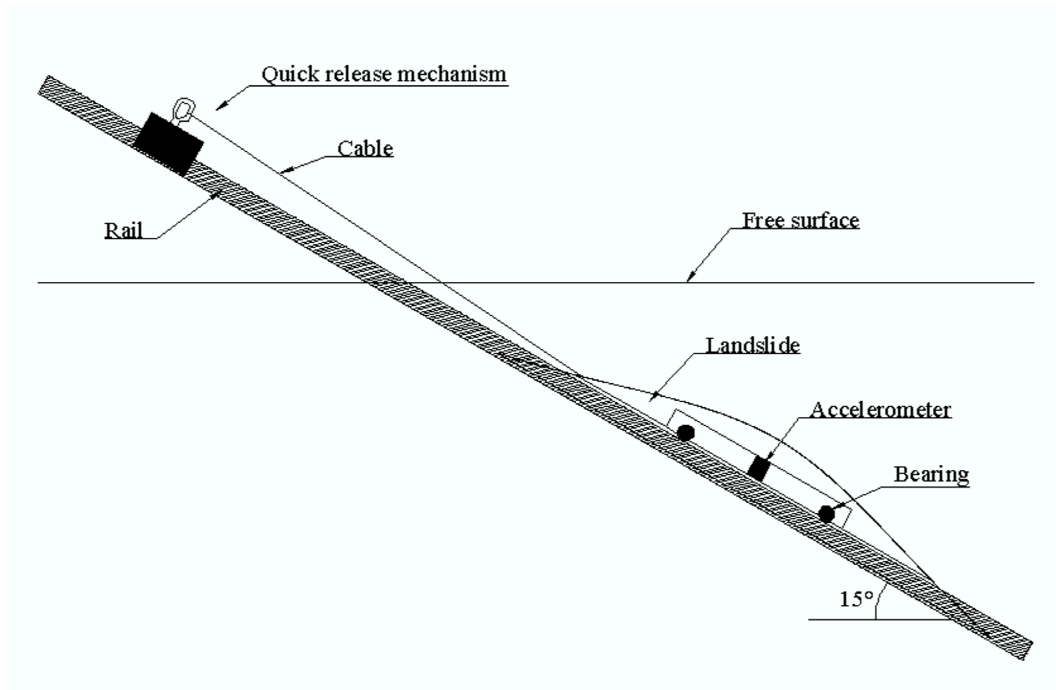


Figure 3:

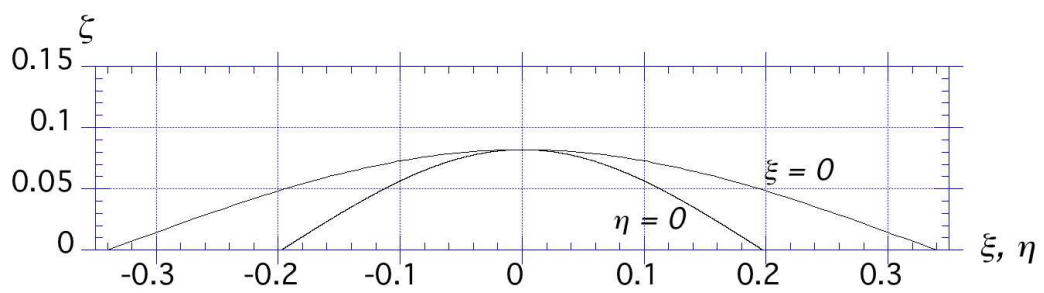


Figure 4:

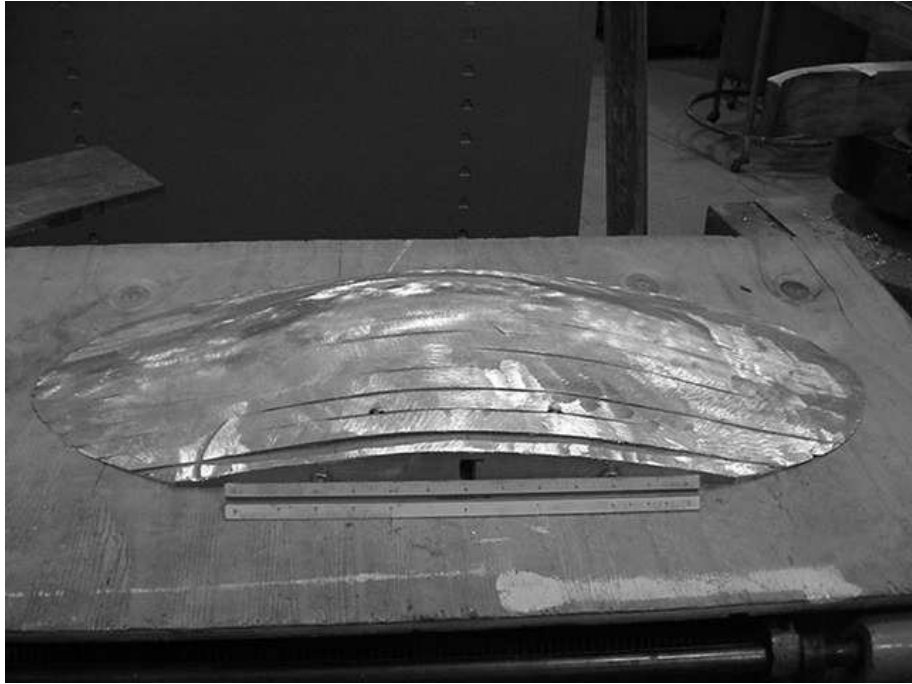


Figure 5:

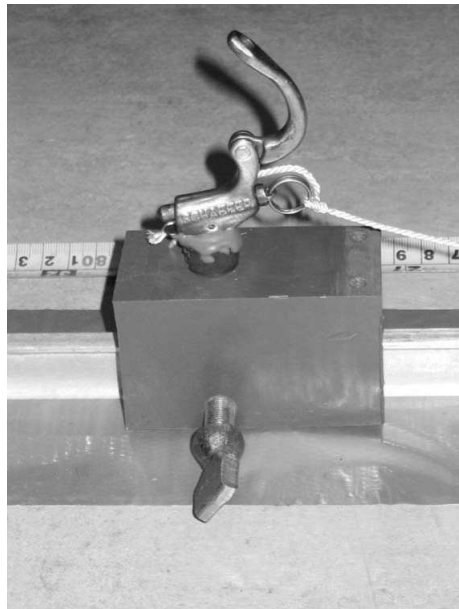


Figure 6:

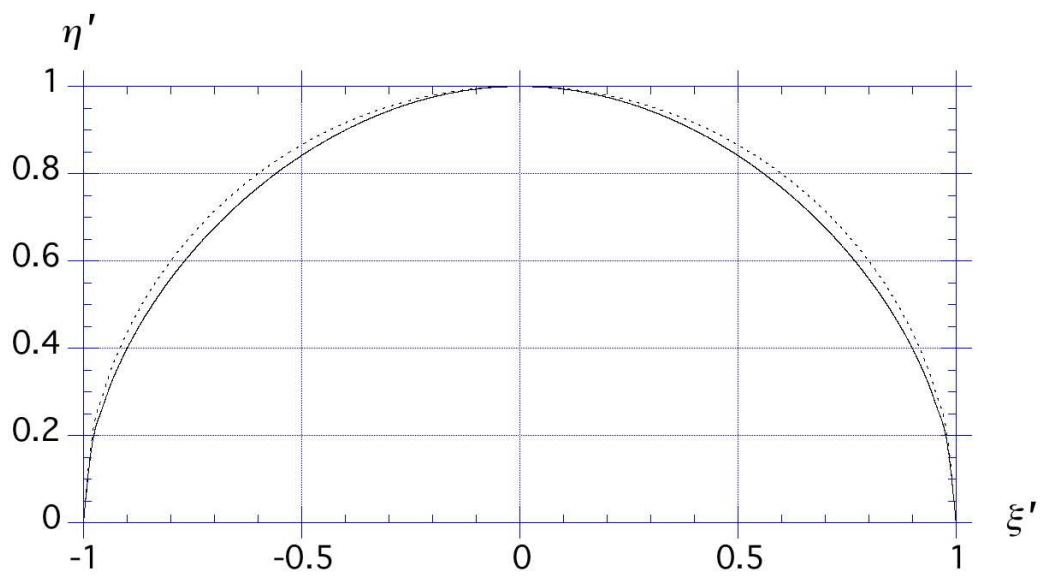


Figure 7:

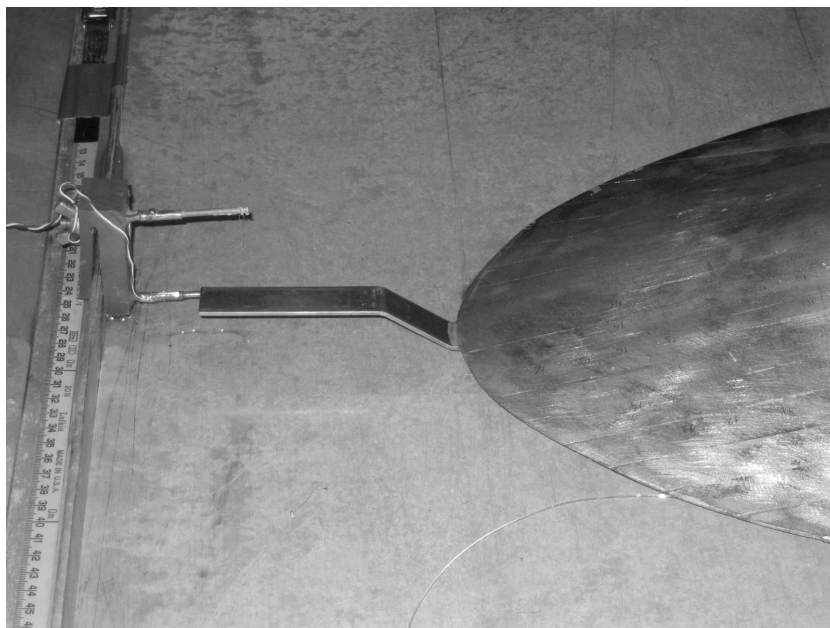


Figure 8:

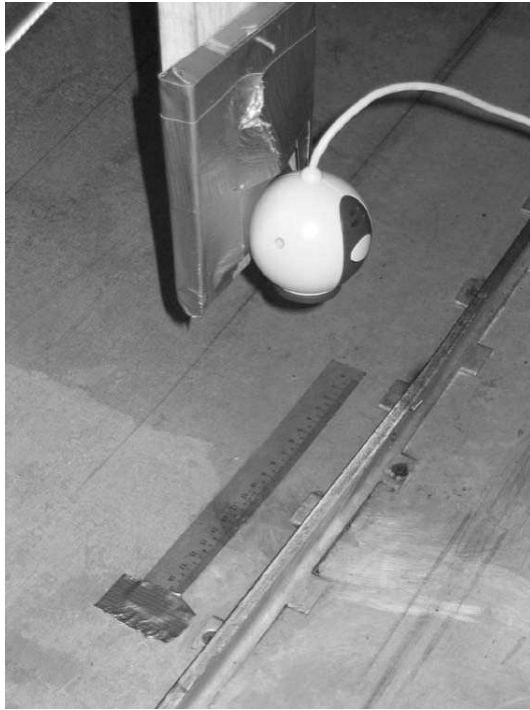


Figure 9:

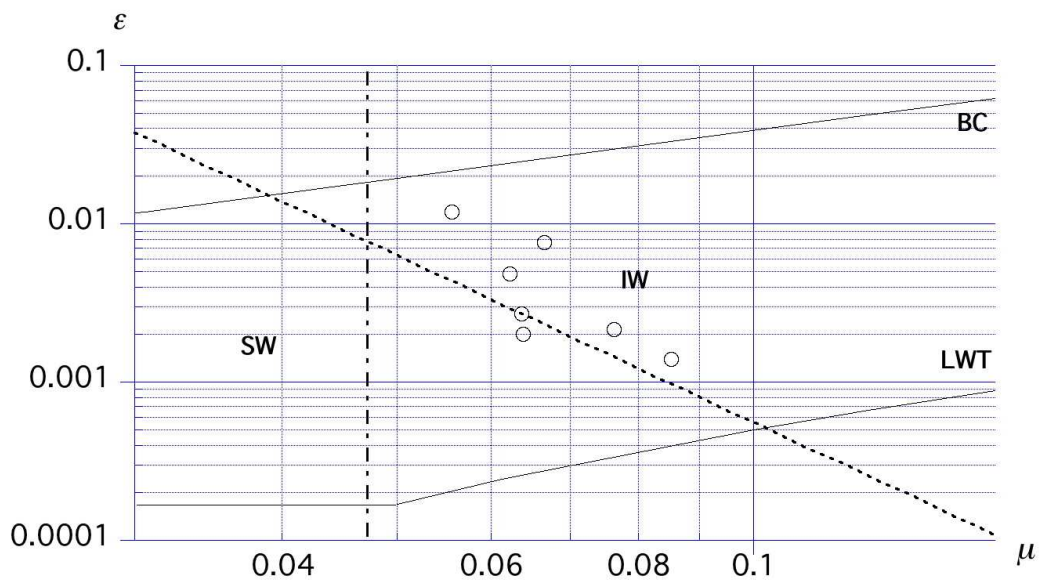


Figure 10:

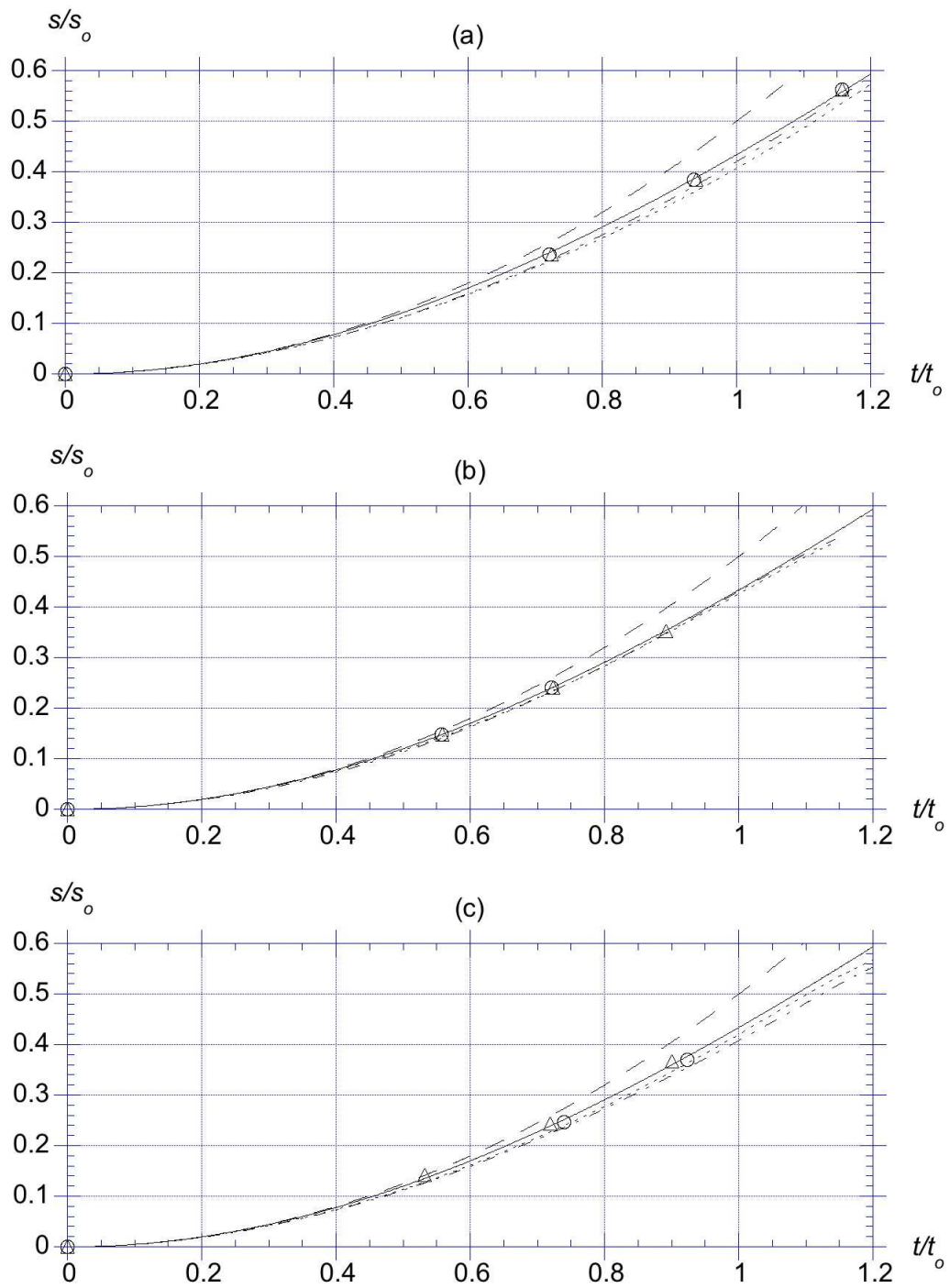


Figure 11:

(a)



(b)



Figure 12:

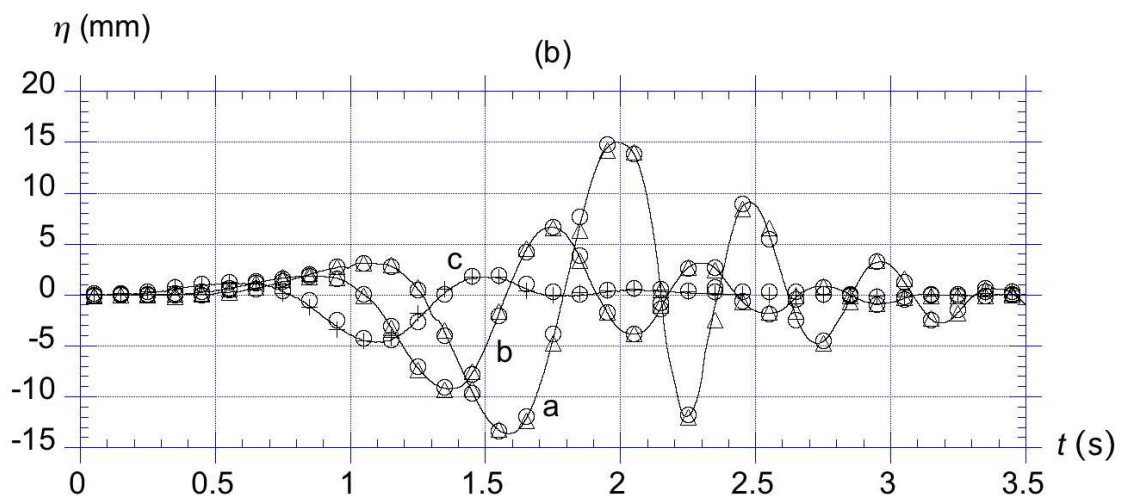
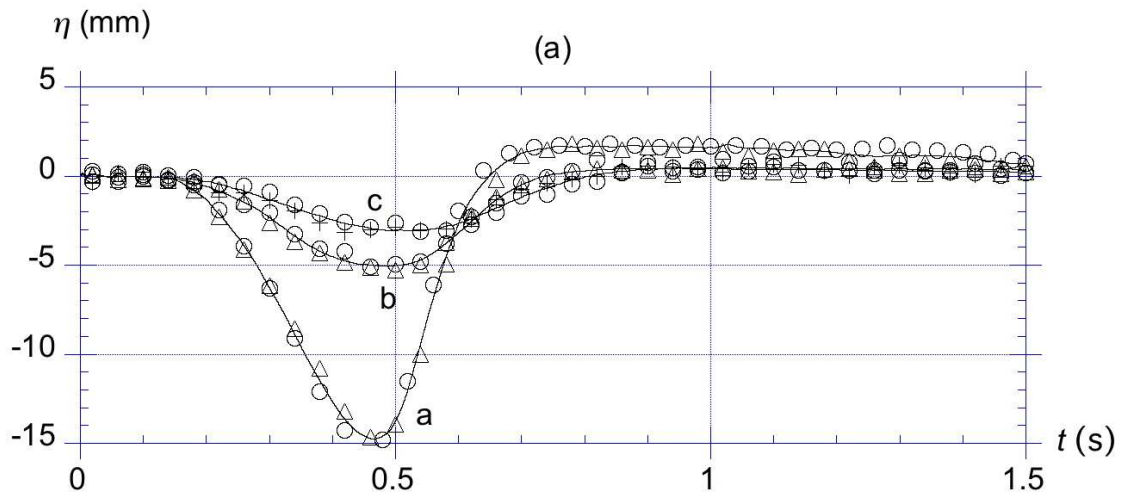


Figure 13:

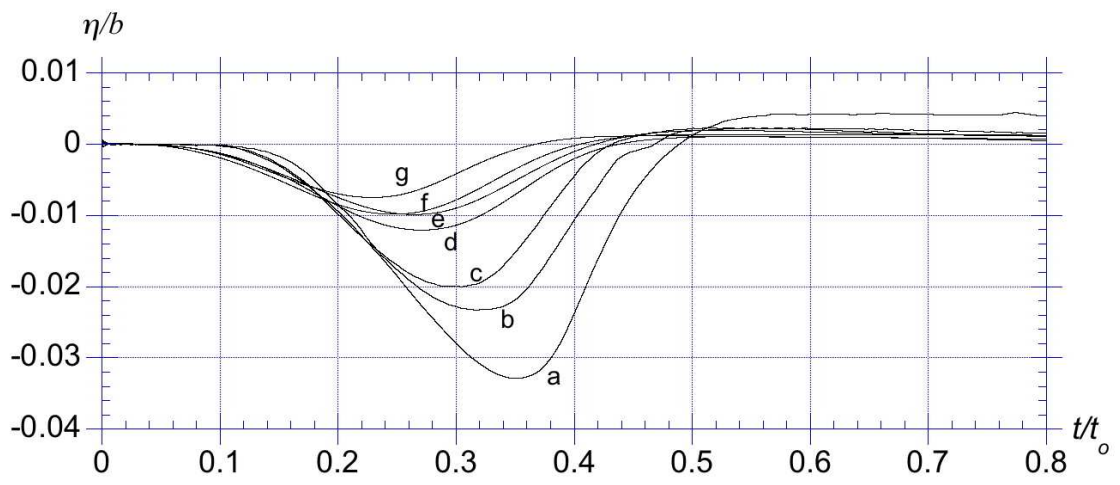


Figure 14:

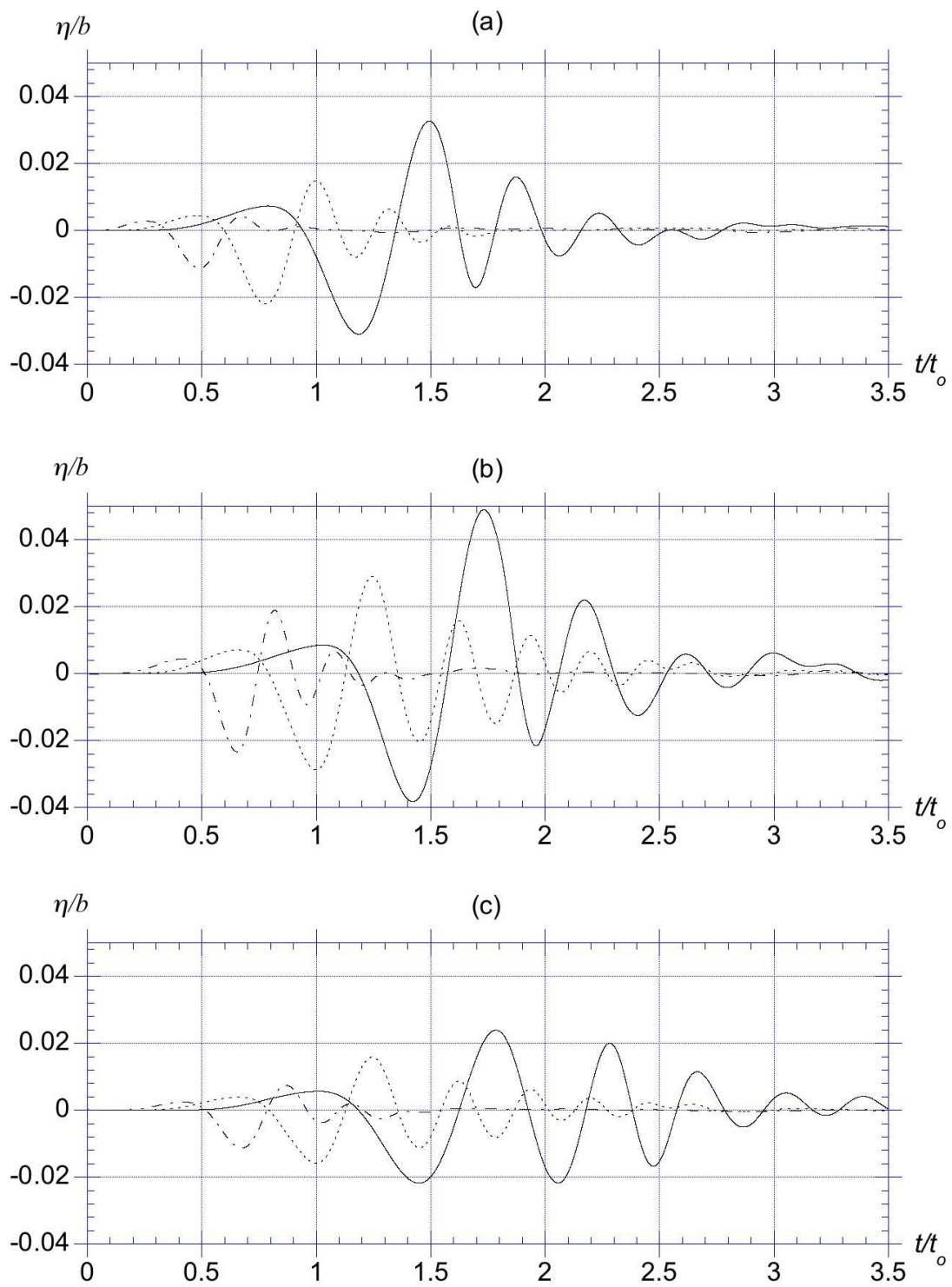


Figure 15:

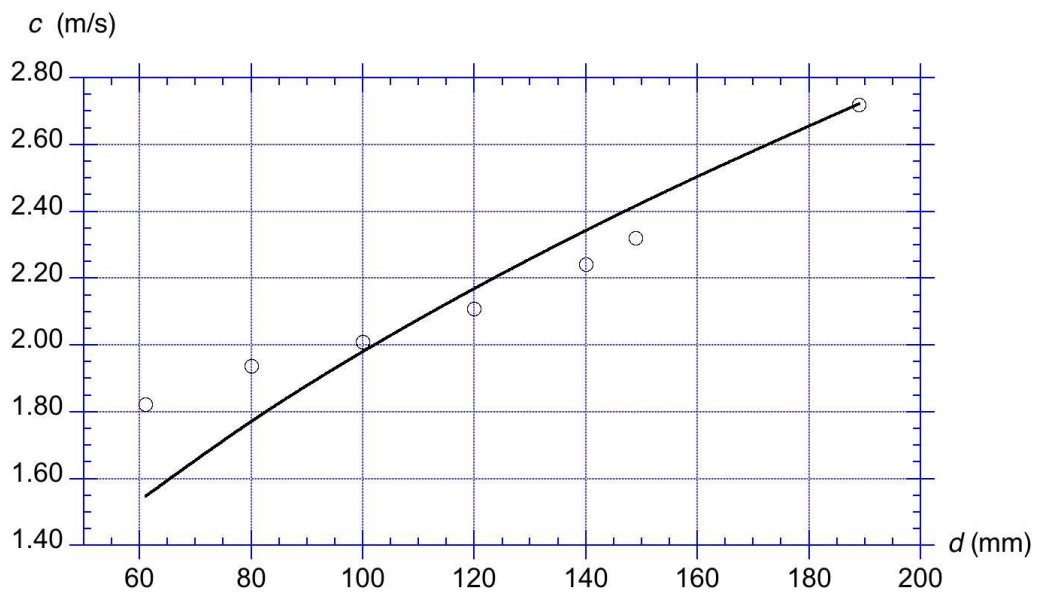


Figure 16:

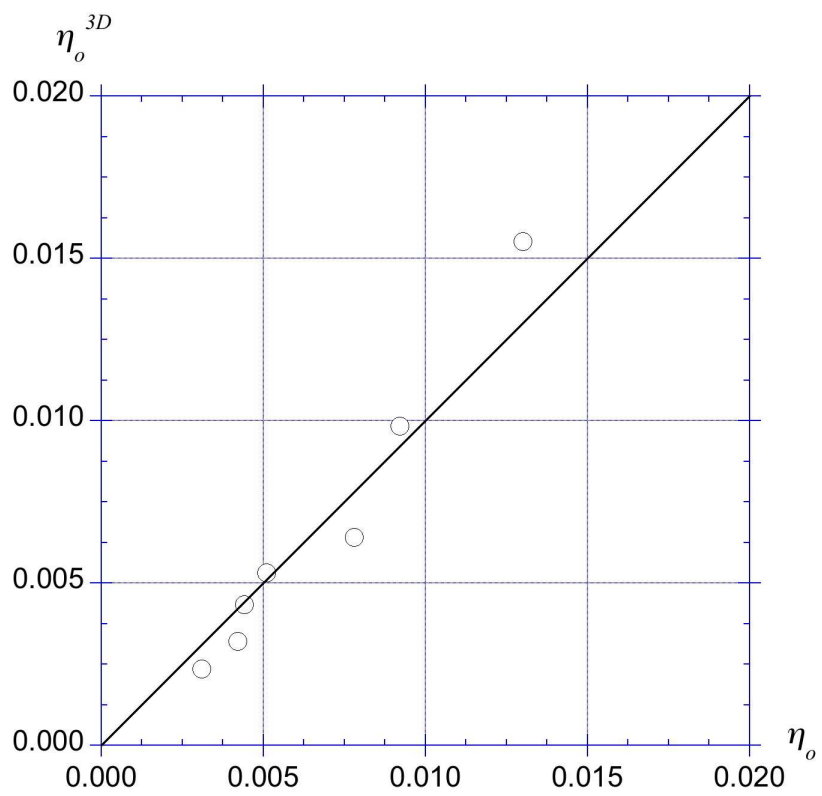


Figure 17:

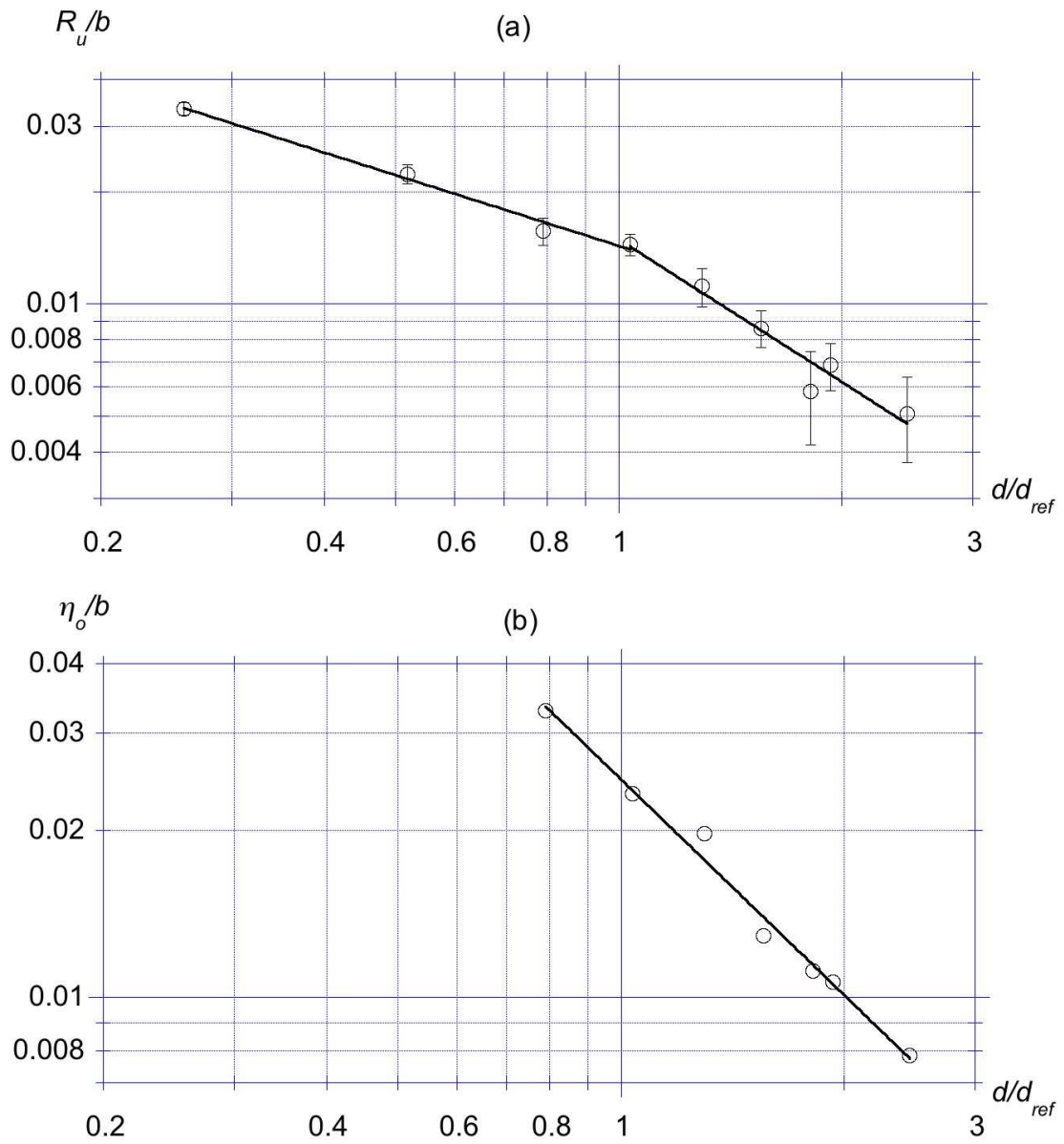


Figure 18: